SID 67-498

STUDY OF APOLLO WATER IMPACT

FINAL REPORT

VOLUME 4

COMPARISON WITH EXPERIMENTS

(Contract NAS9-4552, G.O. 5264)

May 1967

Prepared by

J. P. D. Wilkinson
(Author)

Approved by

F. C. Hung
Program Manager
Structures and Materials

L. A. Harris
Assistant Manager
Science and Technology

NORTH AMERICAN AVIATION, INC.
SPACE DIVISION

SID 67-498

STUDY OF APOLLO WATER IMPACT

FINAL REPORT

VOLUME 4

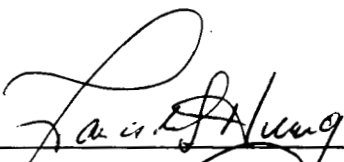COMPARISON WITH EXPERIMENTS

(Contract NAS9-4552, G.O. 5264)

May 1967

Prepared by

J. P. D. Wilkinson
(Author)

Approved by

F. C. Hung
Program Manager
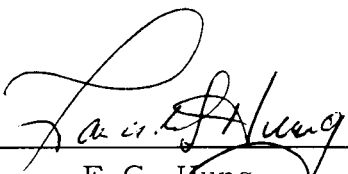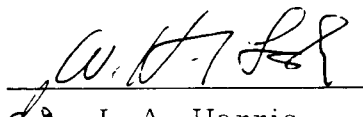Structures and Materials

L. A. Harris
Assistant Manager
Science and Technology

NORTH AMERICAN AVIATION, INC.

SPACE DIVISION

FOREWORD

This report was prepared by North American Aviation, Inc., Space Division, under NASA Contract NAS9-4552, for the National Aeronautics and Space Administration, Manned Space Flight Center, Houston, Texas, with Dr. F.C. Hung, Program Manager and Mr. P.P. Radkowski, Assistant Program Manager. This work was administered under the direction of Structural Mechanics Division, MSC, Houston, Texas with Dr. F. Stebbins as the technical monitor.

This report is presented in eleven volumes for convenience in handling and distribution. All volumes are unclassified.

The objective of the study was to develop methods and Fortran IV computer programs to determine by the techniques described below, the hydro-elastic response of representation of the structure of the Apollo Command Module immediately following impact on the water. The development of theory, methods and computer programs is presented as Task I Hydrodynamic Pressures, Task II Structural Response and Task III Hydroelastic Response Analysis.

Under Task I - Computing program to extend flexible sphere using the Spencer and Shiffman approach has been developed. Analytical formulation by Dr. Li using nonlinear hydrodynamic theory on structural portion is formulated. In order to cover a wide range of impact conditions, future extensions are necessary in the following items:

a. Using linear hydrodynamic theory to include horizontal velocity and rotation.

b. Nonlinear hydrodynamic theory to develop computing program on spherical portion and to develop nonlinear theory on toroidal and conic sections.

Under Task II - Computing program and User's Manual were developed for nonsymmetrical loading on unsymmetrical elastic shells. To fully develop the theory and methods to cover realistic Apollo configuration the following extensions are recommended:

a. Modes of vibration and modal analysis.

b. Extension to nonsymmetric short time impulses.

c. Linear buckling and elasto-plastic analysis

These technical extensions will not only be useful for Apollo and future Apollo growth configurations, but they will also be of value to other aeronautical and spacecraft programs.

The hydroelastic response of the flexible shell is obtained by the numerical solution of the combined hydrodynamic and shell equations. The results obtained herein are compared numerically with those derived by neglecting the interaction and applying rigid body pressures to the same elastic shell. The numerical results show that for an axially symmetric impact of the particular shell studied, the interaction between the shell and the fluid produces appreciable differences in the overall acceleration of the center of gravity of the shell, and in the distribution of the pressures and responses. However the maximum responses are within 15% of those produced when the interaction between the fluid and the shell is neglected. A brief summary of results is shown in the abstracts of individual volumes.

The volume number and authors are listed on the following page.

The contractor's designation for this report is SID 67-498.

INDEX FOR FINAL REPORT

"Apollo Water Impact"

ABSTRACT

In this volume, the pressures, vehicle accelerations, and vehicle velocities which have been obtained in the theoretical analyses described in Volumes 2 and 3 are compared with full-scale and quarter-scale experimental results. In addition, empirical expressions in the form of polynomials are derived by a least squares fit of the full-scale pressure profiles. In comparison with the full-scale test results it is observed that low-pitch angles give higher accelerations, whereas high-pitch angles give lower accelerations. The effect of high horizontal velocity is also seen to result in lower accelerations. It may be that a combination of high pitch angle and high horizontal velocity produces a wedge-like impact, where the impact takes place on the toroidal portion of the heat shield.

TABLE OF CONTENTS

LIST OF ILLUSTRATIONS

INTRODUCTION

An extensive program of Water Impact Tests of the Apollo Command Module has been carried out in support of the Apollo Program. Full-scale and 1/10-scale testing was conducted by North American Aviation, Inc., Space and Information Systems Division, and 1/4-scale tests were conducted by NASA at their Langley Research Center. Analysis of the data from the above tests has been carried out by the Space and Information Systems Division of North American Aviation, Inc., and has yielded experimental values of pressure and acceleration versus location, time, wetted radius, and other parameters. This analysis showed agreement between the data from the various scaled tests and correlation of loads, determined from acceleration data, and the pressure data. The results of these tests are reported in several North American Aviation, Inc., internal letters and were presented to the NASA in a series of briefings.

This Volume is divided into two parts. The first discusses the full scale experiments and comparisons with the theoretical studies of Volumes 2 and 3. The second part is concerned with the comparison of the theoretical results and the 1/4-scale tests conducted at the NASA Langley Research Center.

FULL SCALE TESTS

Among the numerous full scale water impact tests conducted at North American Aviation, Inc. , there were many in which the Apollo Command Module impacted upon the water with small pitch angle (so that the point of impact was situated on the heat shield), and with a very low horizontal velocity. The vertical and horizontal velocities and the pitch angles of these tests are shown in Table 1. In each test, accelerations and velocities of the vehicle were measured and the pressures were recorded at certain points on the heat shield.

Vehicle Acceleration

The acceleration of the vehicle center of gravity was measured during all drop tests. In Table I we show the recorded maximum acceleration and its time of occurrence. The individual points for most drop tests are plotted in Figures 1a and 1b. In Figure 1a, we show the corresponding drop number, and the pitch angle at which the vehicle impacted. In Figure 1b we show by the shaded areas the trend produced by the difference in pitch angle during each drop. It is observed that low pitch angles give higher accelerations, whereas high pitch angles give lower accelerations. The effect of high horizontal velocity is also seen to result in lower accelerations. It may be that a combination of high pitch angle and high horizontal velocity produces a wedge-like impact, where the impact takes place on the toroidal portion of the heat shield.

The solid curve represents the maximum acceleration predicted by the rigid-body theory of Volume 2, where no interaction is included. We observe that these results are consistently lower than the experimental results, except for those where the impact may have been wedge-like.

We have also plotted the point of maximum acceleration predicted by the hydroelastic interaction theory of Volume 3. This point falls directly on the main trend of measured accelerations when the pitch angle is zero. This indicates that the interaction between the fluid and the structure is important in determining the acceleration of the center of gravity.

The time of occurrence of the maximum acceleration of the center of gravity is shown in Figure 2 for various vertical impact velocities. Here, the experimental results are rather widely scattered. The rigid-body theory predicts times which are somewhat less than the recorded times, while the hydroelastic interaction theory predicts a time even shorter than this. It is

possible that while the maximum accelerations could be easily read off the raw data recordings, the times at which they occur are more difficult to obtain and are more subject to an error of a few milliseconds.

Vehicle Velocity

During the full scale tests, full camera coverage enabled the velocity of the vehicle to be monitored during the impact. In Figure 3 is shown the velocities of the vehicle after impact for many of the drop tests. A line of marking the time of the maximum acceleration is also shown. Figure 4 shows the corresponding theoretical results. Here, it appears that the maximum acceleration occurs much sooner than in the experimental results, although the general shape of the velocity curves is not much different. The discrepancy in the time of occurrence of the maximum acceleration is attributed to the fact that is is very difficult to measure the precise time at which the maximum occurs.

Pressure Distributions

During the water impact tests conducted on the full scale Apollo Command Module, various measurements of the pressures due to the impact were taken among these tests, there were many in which the Apollo command module impacted upon the water with small pitch angle (so that the point of impact was situated on the heat shield) and with a very low horizontal velocity. The vertical and horizontal velocities and the pitch angle of these tests are shown in Table 1. In each test, the pressures at certain points on the heat shield were recorded.

A typical pressure distribution P on the heat shield at any particular instant of time t is shown in Figure 5. The distribution is a function of impact velocity V_o, time t, and radius r from the impact point. In Figure 5, the pressure distribution is axially symmetric with respect to the impact point. The pressure is a maximum at or near the free water surface, and is minimum at the point of impact. The pressure is axially symmetric only when the horizontal velocity is zero. When a horizontal velocity component H is present, the profile is slightly skewed, as shown in Figure 6. Here, the maximum pressures occur near the free water surface at the front of the capsule. Although some drop tests were concerned with large horizontal velocities, these tests indicated that the horizontal velocity component has little effect on the overall pressure distribution. The vertical velocity component was the parameter of primary importance. Furthermore, rather large scatter was observed in all pressure readings. Consequently, only those drops with small horizontal velocity will be considered in this report.

In Figures 7 through 14 are given the observed pressure readings for the drop tests 83 through 90. They are obtained from References 7 and 8.

In this section, we shall use some of these measurements to derive an empirical expression for the pressure profiles. Furthermore, a comparison of some of the experimentally observed quantities will be made with the theoretically derived results of the preceding Sections of this report.

The most reliable pressure readings appear to be those recording the maximum pressure near the edge of the wetted surface. We denote these maxima by p_m. By using the results of the full scale drop tests described in References 1 to 11, we can derive, by means of a least squares surface fit of the experimental data, an expression for p_m as a function of initial impact velocity V_o and time t. Thus, we fit a fifth degree polynomial surface of the type

$$\frac{1}{10} p_m (t, V_o)$$

$$= a_1 + a_2 T + a_3 V_o + a_4 T^2 + a_5 TV_o + a_6 V_o^2$$

$$+ - - - - - - - - - - + a_{21} V_o^5 \tag{1}$$

where

$$T = 1000 t$$

The result of this least squares fit is shown in Figures 15 through 21. In Figure 15, some typical curves of p_m as a function of time are shown for various initial impact velocities. In addition, the polynomial coefficents $a_1, a_2, \ldots, a_{21}$ are exhibited. Figures 4 through 9 show in detail p_m (t) for each pertinent initial velocity V_o, as well as the corresponding experimental points.

A slight modification in the polynomial was then made so that the curves would not overlap, as they do in Figure 15. The result of the new polynomial surface is shown in Figure 22, together with the polynomial coefficients $a_1, a_2, \ldots, a_{21}$. The detailed results are given in Figures 23 through 28, together with the original data points.

A second quantity which could be easily obtained from the experimental data was the radial distance from the impact at which the maximum pressure p_m occurs. We have already observed, from the foregoing theoretical work of Volumes 2 and 3 of this report, that the pressures are maximum at or near the edge of the wetted surface. Thus the radial distance at which p_m occurs can be directly compared with this theoretical measurement. Let us devote the radius by r_m. By fitting a fifth degree polynomial surface of the type

$$r_m(t, V_o) = b_1 = b_2 T + b_3 V_o + b_4 T^2 + b_5 T V_o + b_6 V_o 2 + \ldots \ldots + b_{21} V_o 5$$

where   (2)

$$T = 1000\, t,$$

we obtain the curves of Figure 29. There the coefficients b_1, b_2, . . ., b_{21} are also shown. In Figures 30 through 34 the detailed results obtained from the polynomial are compared with the original data points obtained from the scale tests.

A slight modification of the polynomial surface renders lines which do not overlap as they do in Figure 29. This polynomial is illustrated in Figure 35. The detailed curves and their comparison with the original data points are shown in Figures 36 through 41.

For comparison with theoretical results, we illustrate in Figure 42 the radial distance obtained from the rigid-body theory (no interaction) of Volume 2. It is observed that the pressure pulse does not travel as rapidly across the shell as the experimental results indicate. This disagreement can be explained on the basis that the theoretical results are obtained from a linearized theory which neglects the effect of the splash. This splash may have the effect of causing the pressure transducers to register at an earlier time than the theoretical results would predict.

In Figure 43, we have combined the results of Figures 22 and 35. From this Figure can be derived p_m and V_m at any time, given the initial impact velocity.

An empirical expression for the pressure profile at any instant of time may be derived by using the polynomial expressions $p_M(t, V_o)$ and $r_M(t, V_o)$, together with the estimates of vehicle acceleration, A, derived on the basis of rigid-body entry in a previous section.

At instants of time immediately after the impact, the profile will be as illustrated in Figure 5. Let us assume a parabolic variation of p along the radius r.

Thus

$$p = p_o + br + cr^2 \tag{3}$$

where p_o is the unknown stagnation pressure at the impact point. But since $\dfrac{dp}{dr} = 0$ at $r = 0$ because of symmetry are $p = p_M$ at r_M, we find that

$$p = p_o + \frac{p_m - p_o}{r_M^2} r^2$$

the total upward force F on the vehicle due to this pressure is

$$F = \int_o^{r_M} 2\pi r p \, dr = \frac{\pi}{2} r_M{}^2 \left(p_m + p_o \right)$$

(4)

(5)

But

$$F = \frac{W}{a} A$$

(6)

and so

$$p_o = \frac{2WA}{\pi g r_M{}^2} - p_M$$

(7)

After a certain time has elapsed, it will be found that $p_o < 0$. Of course a pressure less than zero is not possible if we assume that no cavitation occurs. For pressures subsequent to that time, a new estimate can be made by assuming that

$$p = p_m \left(\frac{r}{r_m} \right)^n$$

(8)

where n is an exponent to be determined.

Then, because

$$F = \int_o^{r_m} 2 \, r p_m \left(\frac{r}{r_m} \right) dr = \frac{WA}{g}$$

(9)

we find that

$$n = 2 \left[\frac{\pi p_m g r_m}{WA} - 1 \right]$$

(10)

and

$$p = p_m \left(\frac{r}{r_m} \right)^{2 \left[\frac{\pi p_m g r_m}{WA} - 1 \right]}$$

(11)

where A is once again determined from either the experimental results or from the theoretical rigid-body calculations.

By using the values of the acceleration for a rigid body of radius 14. 85 ft. and having an initial impact velocity of 30 fps, we can generate, from Equations (1), (2), (4), (7), and (11), the pressure profiles shown in Figure 44. The overall profile is representative of what is observed exper- imentally, and could itself be used as a forcing function for the purpose of a dynamic analysis of a flexible body during impact. In Figure 45 is illus- trated the theoretical pressure profiles from a rigid body of the same size and having the same initial velocity. It is seen that the agreement between the two derivations is fairly good. The main shortcoming of the linearized theory seems to be that it predicts infinite peak pressures, and also that the speed of propagation of the pressure pulse is somewhat slower than actually observed. These points will be discussed in detail later on.

QUARTER SCALE TESTS

At the NASA Langley Research Center, a series of tests have been conducted covering the vertical axially symmetric impact of a rigid 1/4-scale model of the Apollo Command Module. Additional tests have recently been performed with a 1/4-scale model having a flexible heat shield.

Vehicle Accelerations

Figure 46 shows the measured accelerations of accelerations of the center of gravity of the Langley 1/4-scale rigid model. The model weighed 165 pounds and had a radius of 44. 1 inches. The maximum acceleration is between 5. 95g and 6. 55 g, occurring between 0. 006 seconds and 0. 007 seconds. The corresponding analytical prediction based on rigid-body theory is shown in Figure 47. Here the maximum acceleration is 4. 4g and it occurs at 0. 0075 seconds after the impact. There is a 25% to 33% difference in the results.

Pressure Distributions

Figures 48 and 50 show the experimentally observed pressure profiles acting on a rigid body during impact at 7. 62 fps and 15. 3 fps, respectively. The corresponding theoretical rigid-body results are shown in Figures 49 and 51.

Although direct comparison is difficult, we observe that the general shape of the profiles is the same in each case. However, it appears that the pressures propagate more rapidly than predicted by the theory. This may be explained by the effect of the spray root and displaced water, which was neglected in the analysis.

CONCLUSIONS

Both the full scale and quarter scale experimental results show that the rigid-body theory predicts that the pressure wave propagates a little too slowly. This can be explained by the effect of the nonlinear free surface, which tends to produce pressures on the shell in advance of those predicted on the basis of a planar free surface.

The accelerations of the center of gravity predicted by the rigid-body theory are, in general, smaller than actually measured. However, the hydroelastic theory does predict higher accelerations which fall within the main trend of the full scale tests.

The theoretically obtained pressures, are, in general, within 25 percent of those observed experimentally. Substantial agreement exists between theory and experiment in many areas. Below, we offer a number of comments as to the possible sources of any discrepancies that do exist.

Departures From Reality In The Theory

1. Since the splash has been neglected, and the free surface has been linearized, the pressure peaks may be in same error. In addition, because of the assumption of the planar free surface, the theoretical pressure wave does not propagate as rapidly as that observed in experiments.

2. The effects of compressibility may still play a part in the phenomenon at the edges of the wetted surface.

Possible Sources of Experimental Error

1. The diameter of the pressure transducers appear to be roughly the same size as the characteristic length of the pressure peaks

    near the wetted edge. This may mean that the transducers will not measure the true peaks, but instead will measure an average pressure.

2. There may be some slight hydroelastic effect acting on the transducers themselves.

SUMMARY AND RECOMMENDATIONS

A considerable number of water impact tests have been carried out on both full-scale and 1/10-scale models at the Space and Information Systems Division of North American Aviation. Tests have also been conducted at the Southwest Research Institute, [12] San Antonio, Texas, and at NASA Langley. The data used in this report was taken exclusively from the results of the NAA full-scale drop tests. It is recommended that further study be made of the existing data from all other sources. Although all the data has not been fully documented, it is felt that an analysis of the raw data tapes in existence would be beneficial. Further impact tests could be carried out if, after a detailed inspection of the existing raw data, it is determined that more data is necessary to fill in any experimental gaps.

In this section of the report empirical expressions have been determined from test data for the pressure distribution on the Apollo heat shield during a vertical water impact. In addition, comparisons have been made between the desired theories and the experimental observations of the full scale and quarter scale tests.

REFERENCES

1. Water Impact Test Drop No. 60. Accelerometer and Pressure Transducer Data Report. Test Date 12 December 1963. NAA SID ATO-DE-64-20-58, 29 January 1964.

2. Water Impact Test No. 63. Accelerometer and Pressure Data Report. Test Date 14 January 1964. NAA SID ATO-TD-64-20-A8, 26 May 1964.

3. Water Impact Test No. 65. Accelerometer and Pressure Data Report. Test Date 20 January 1964. NAA SID ATO-TD-64-20-A16, 9 June 1964.

4. Water Impact Test No. 66. Accelerometer and Pressure Data Report. Test Date 22 January 1964. NAA SID ATO-TD-64-20-A13, 28 May 1964.

5. Water Impact Test No. 67. Addendum A, Pressure Data. Test Date 28 January 1964. NAA SID ATO-TD-64-20-93A, Enclosure (1), 11 June 1964.

6. Water Impact Test No. 71. Data Report. Test Date 8 June 1964. NAA SID ATO-TD-64-20-A24, 8 July 1964.

7. Water Impact Test Nos. 83, 84, 85, 86. Data Report. Test Dates 9-10 December 1964. NAA SID ATO-D-TD-65-20-101, 18 January 1965.

8. Water Impact Test Nos. 87, 88, 89, 90. Data Report. Test Dates 15-16 December 1964. NAA SID ATO-D-TD-65-20-103, 25 January 1965.

9. Water Impact Test No. 91. Boilerplate No. 28. Data Report. Test Date 29 January 1965. NAA SID ATO-D-TD-65-20-106, 17 February 1965.

10. Water Impact Test No. 92. Boilerplate No. 28. Data Report. Test Date 9 February 1965. NAA SID ATO-D-TD-65-20-107, 2 March 1965.

11. Water Impact Test No. 93. Boilerplate No. 28. Data Report. Test Date 4 March 1965. NAA SID ATO-D-TD-20-108, 19 March 1965.

12. Baker, W. E., P. S. Westline, L. R. Garza, P. A. Hunter, "Water Impact Studies of Model Apollo Command Module," Southwest Research Institute, San Antonio, Texas, August 1965, p. 148.

- 15 -

Table 1. Test Parameters

| Drop No.	Pitch	VN	VT	Roll	Accel. at C.G.	Time	Type of Heat Shield	
60	-26.3	21.7	0.4	0	9.5		BP-styrofoam btwn Heat Shield & Blkhd.	Fiberglass Heat Shield ↑
61	-18.3	22.0	0.0	0	10.7		BP-styrofoam btwn Heat Shield & Blkhd.	
62	-8.9	25.5	0.5	0	22.6		BP-styrofoam btwn Heat Shield & Blkhd.	
63	-30	25.2	0.0	0	x = 7.2 / Res. = 9.0	0.018 / 0.017	BP-styrofoam btwn Heat Shield & Blkhd.	
64	-17.5	22.0	0.8		11.8		BP-styrofoam btwn Heat Shield & Blkhd.	
65	-27	24.5	32.0	0	9.8		BP-styrofoam btwn Heat Shield & Blkhd.	
66	-20	29.0	0.9	0	x = 19.5 / R = 21.0	0.018	BP-styrofoam btwn Heat Shield & Blkhd.	
67	-15	30.0	0.0	0	Res. = 19.0	0.011	BP-styrofoam btwn Heat Shield & Blkhd.	
68	-26	24.0	32.0	0	x = 6.5 / Res. = 8.0	0.017	BP-styrofoam btwn Heat Shield & Blkhd.	
71	0	32	0.0	0	x = 34.2 / Res. = 34.8	0.030	BP-styrofoam btwn Heat Shield & Blkhd.	
75	-9	10.6	1.5	180	x = 4.1 / Res. = 4.3	0.040	BP-⎫ Fiberglass H/S & ring protruding from inner structure floor. Inside ring, a gap existed between inner surface of H/S & outer surface of B/H. Tested following configurations:	
76	-9.6	14.5	0.0	173	x = 8.1 / Res. = 8.8	0.021	BP-⎪ a. 4.0 in. gap - filled with styrofoam	
77	-9.5	20.5	0.0	175	x = 17.2 / Res. = 17.6	0.015	BP-⎪ b. 0.8 in. open gap, with 3.2 in. styrofoam c. 4.0 in. gap - no styrofoam	
78	-10.6	24.8	0.0	175	Not Available		BP-⎭ d. Inner B/H cut out.	
79	-9.5	29.6	0.0	180	x = 33.3 / Res. = 34.3	0.015	BP-	
80	-21.3	34.0	44.5	180	Res. = 20	0.020	BP-	
81	-10.3	18.5	0.0	184	x = 8.7 / Res. = 8.8	0.048	BP-Moses bump	
82	-23.0	35.0	42.0	180	x = 15.5 / Res. = 16.1	0.044 / 0.043	BP-Moses bump	
83	-13.0	9.0	0.25	0	x = 2.75 / Res. = 2.81	0.016	BP	
84	-15.0	16.0	2.0	0	x = 3.5 / Res. = 4.35	0.014	BP	
85	-13.6	20.0	~0.0	0	x = 11.5 / Res. = 12.8	0.015 / 0.016	BP	
86	-14.8	24.5	0.5	0	x = 14.1 / Res. = 15.0	0.011	BP	
87	-14.7	9.0	3.5	0	Res. = 4.35	0.020	BP	
88	-14.3	17.0	~0.0	0	x = 5.7 / Res. = 6.4	0.019 / 0.013	BP	
89	-15.0	21.0	2.5	0	x = 9.0 / Res. = 9.7	0.015	BP	
90	-14.4	24.0	-0.0	0	x = 13.0 / Res. = 14.1	0.015	BP	Fiberglass Heat Shield ↓
91	-29.0	29.6	28.2	185	x = 6.4 / Res. = 6.5	0.0315 / 0.0310	BP 28- Modified S/C aft H/S and B/H. H/S beefed up by addition of bonded steel doublers on inner & outer face-sheets. Doublers varied in thickness from 0.020 in. to 0.042 in. The 0.80 in. gap between the H/S & B/H filled with TG15000, $\rho = 15$ lb/ft^3	
92	-19.6	33.6	35.5	180	x = 20.0 / Res. = 20.6	0.015	BP 28-Same H/S as Drop No. 91	
93	-19.3	34.3	38.0	180	Res. = 20.0	0.013	BP 28-Same H/S as Drop No. 91	
98	-46.6	29.2	38.4	0	Estimated less than 5.0		BP 12A-Modified BP 2 type H/S ⎫	
100	-41.0	30.0	45.1	0	Res. = 5.1	0.137	SC 007-H/S facesheets stepped 0.0.42 in., 0.022 in., 0.012 in. ⎪	
101	-13.0	29.3	40.5	180	x = 22.0 / Res. = 22.5	0.010	BP 28-H/S chem-milled facesheets & S/C honeycomb core Facesheets stepped 0.050, 0.030, 0.020 in. ⎬ Additional mathematical smoothing - results in up to 5 g's less peak acceleration.	
102	-15.2	34.2	38.9	180	x = 25.0 / Res. = 26.6	0.010	SC 007-Same type H/S as Drop No. 101 ⎪	
103	-44.4	31.2	46.9	0	Estimated less than 10.0		SC 2S-1-Dual footprint H/S. Brazed doublers on facesheets ⎪	
104	-13.2	34.3	39.2	181	x = 26.3 / Res. = 28.0	0.010	SC 2S-1-Single footprint-chem-milled facesheets & honeycomb core ⎭	
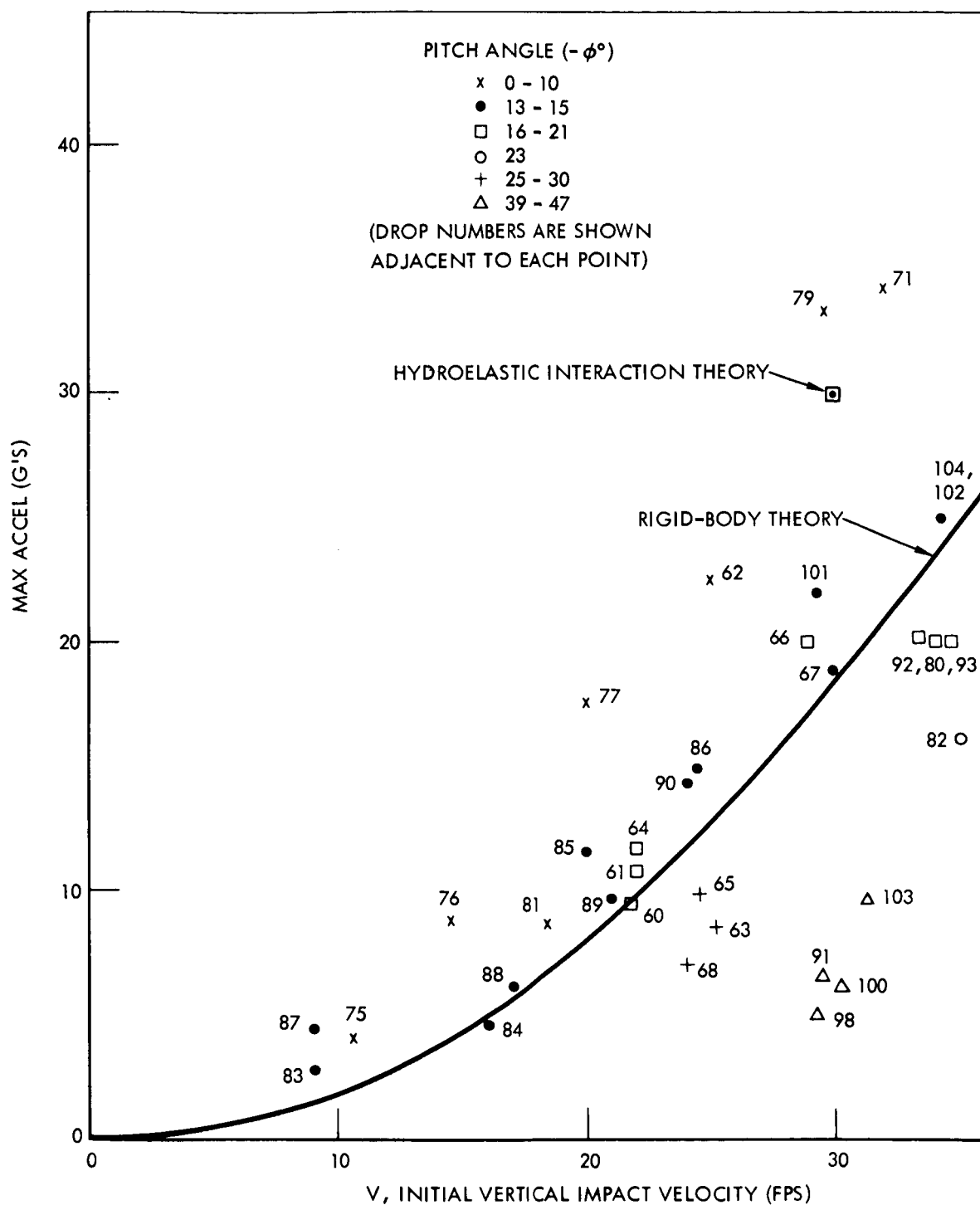
Figure 1a. Full Scale Experimental and Theoretical Maximum Accelerations.
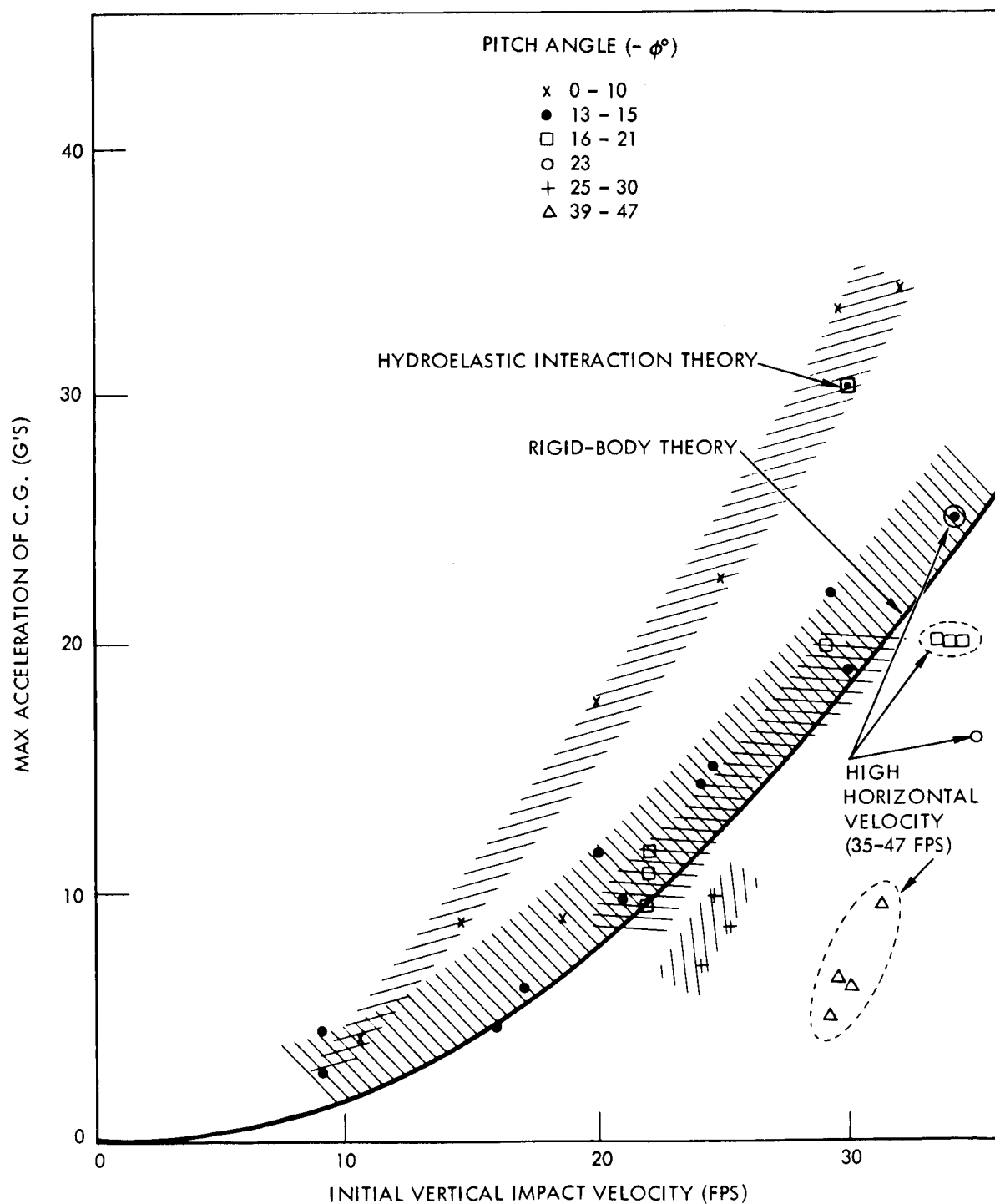
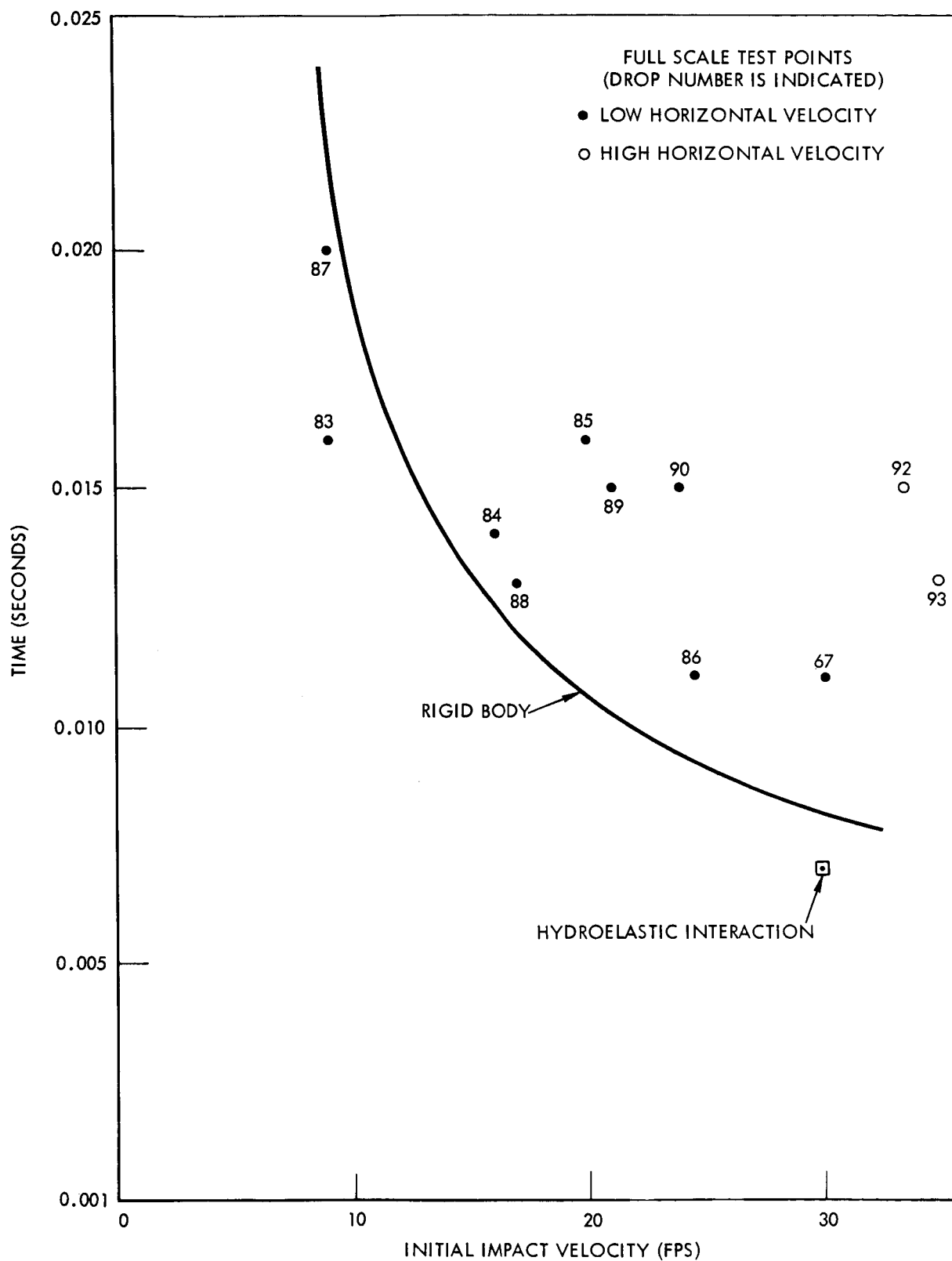Figure 1b. Full Scale Experimental and Theoretical Maximum Accelerations.

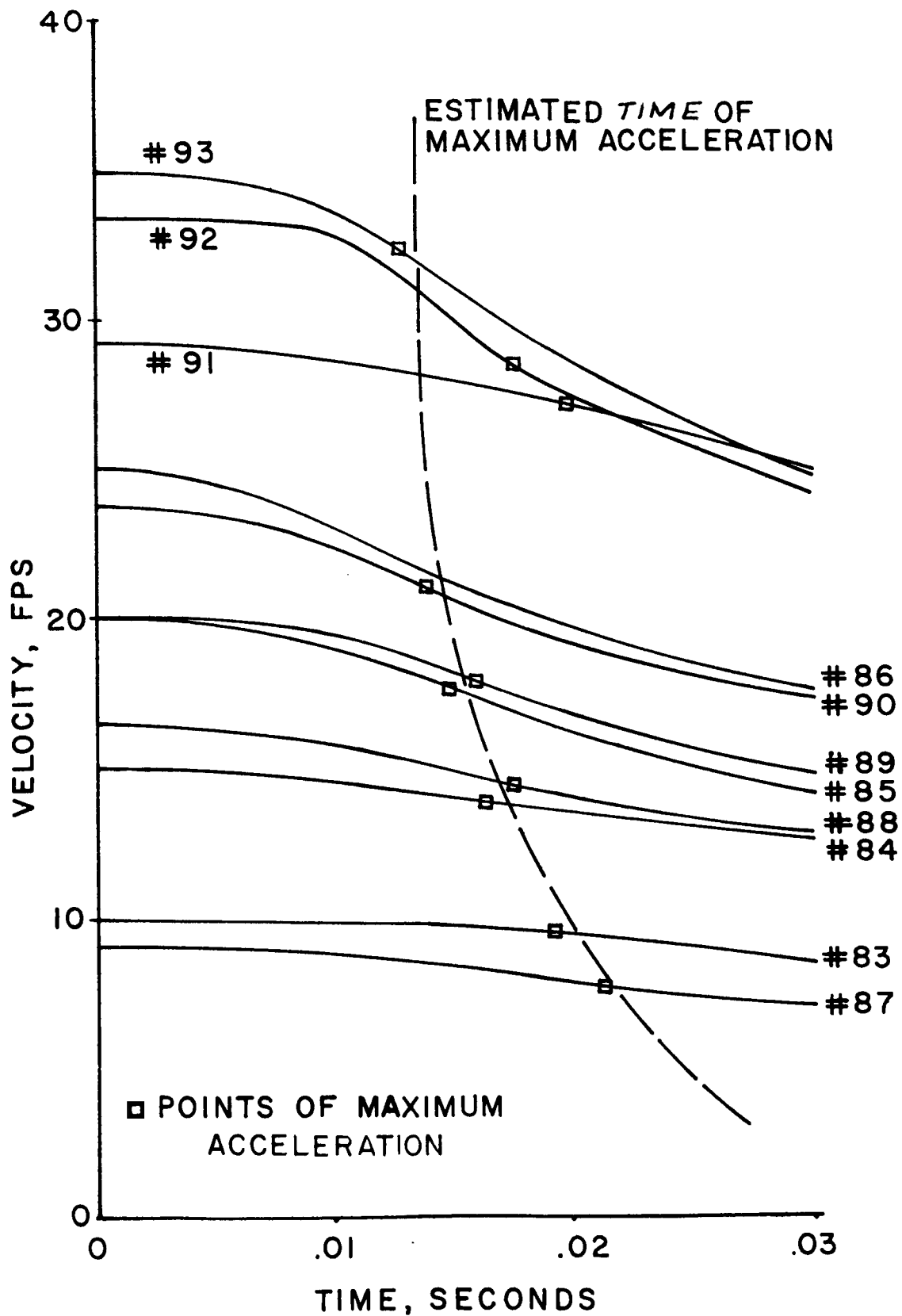Figure 2.   Time of Occurrence of Maximum Accelerations.

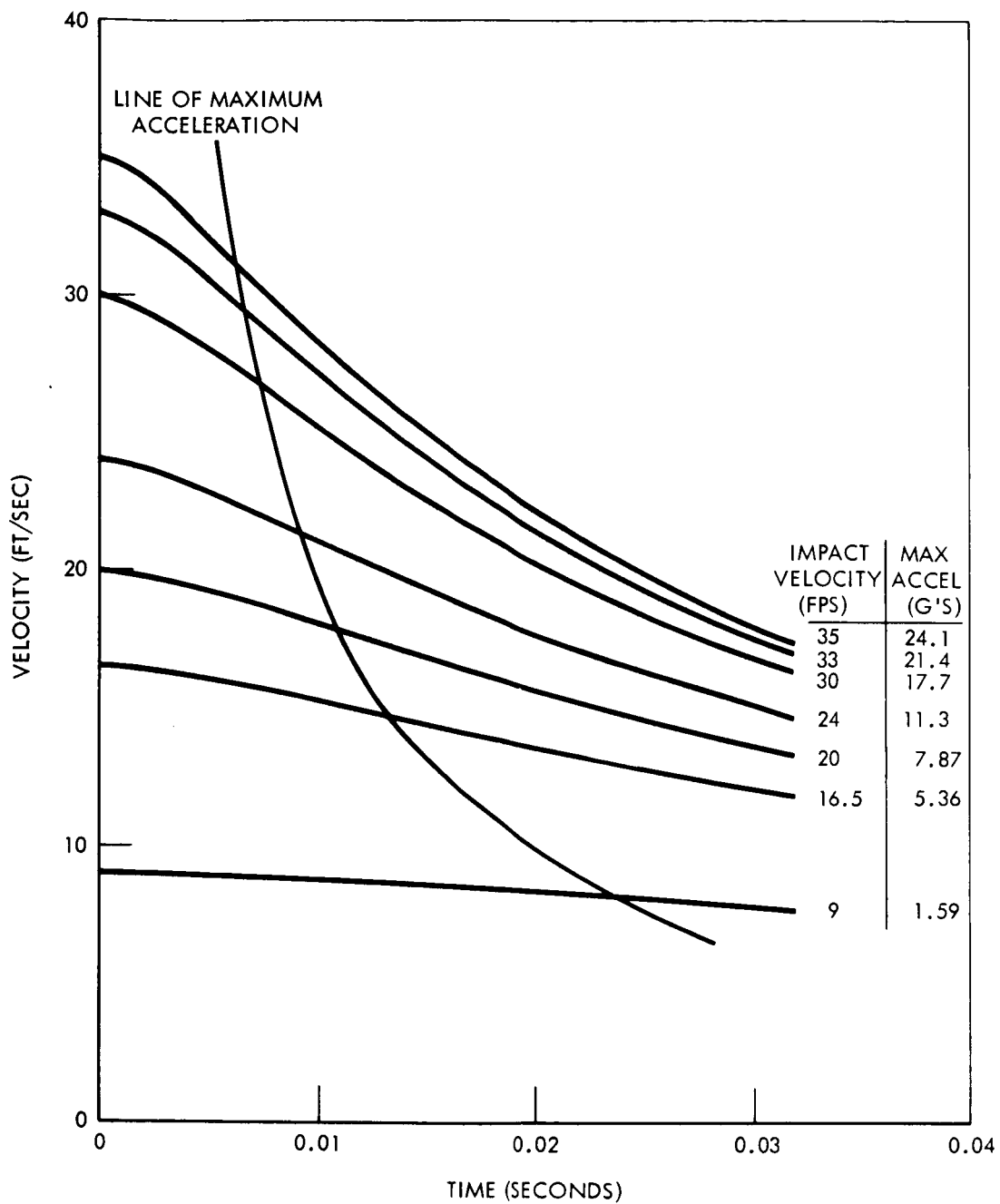Figure 3. Experimental Velocities During Impact.
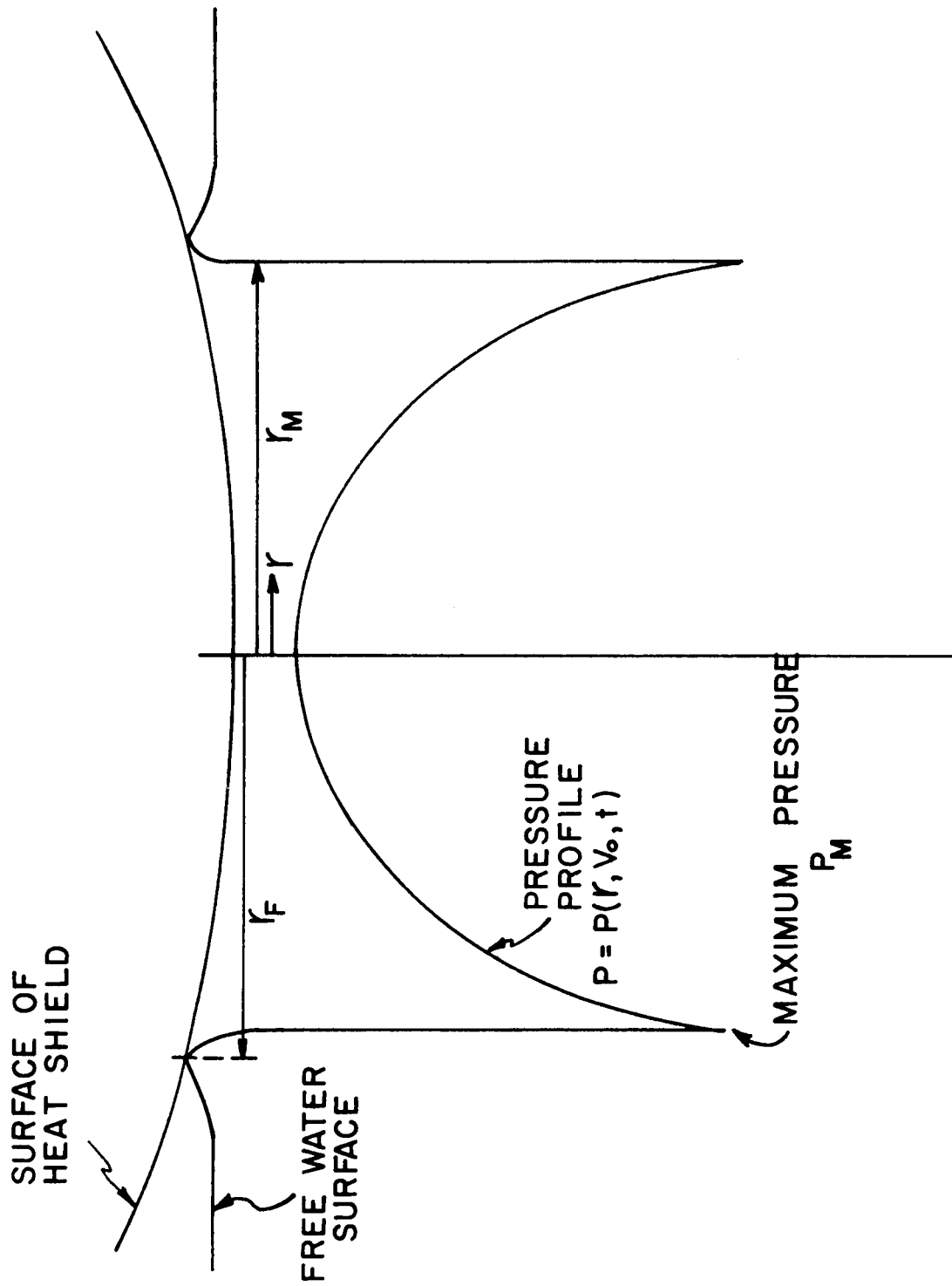
Figure 4.   Theoretical Velocities During Impact.

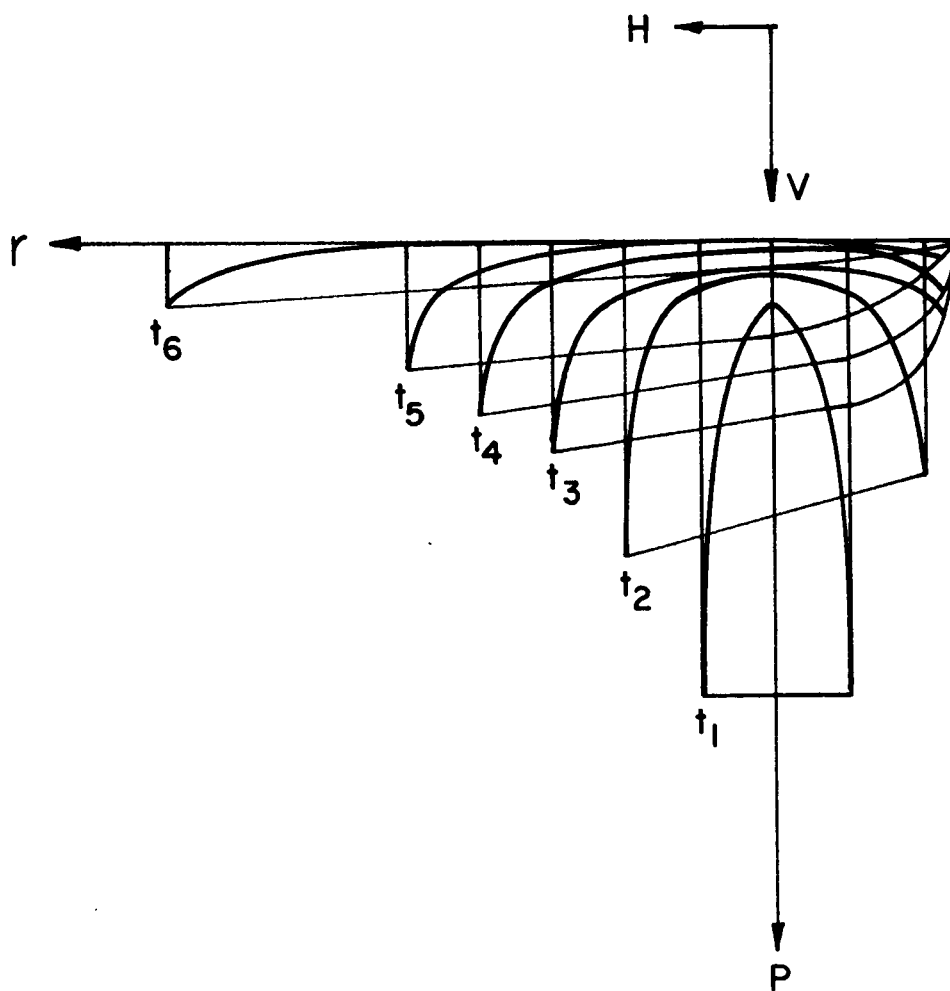Figure 5. Typical Pressure Profile for an Axially Symmetric Impact.

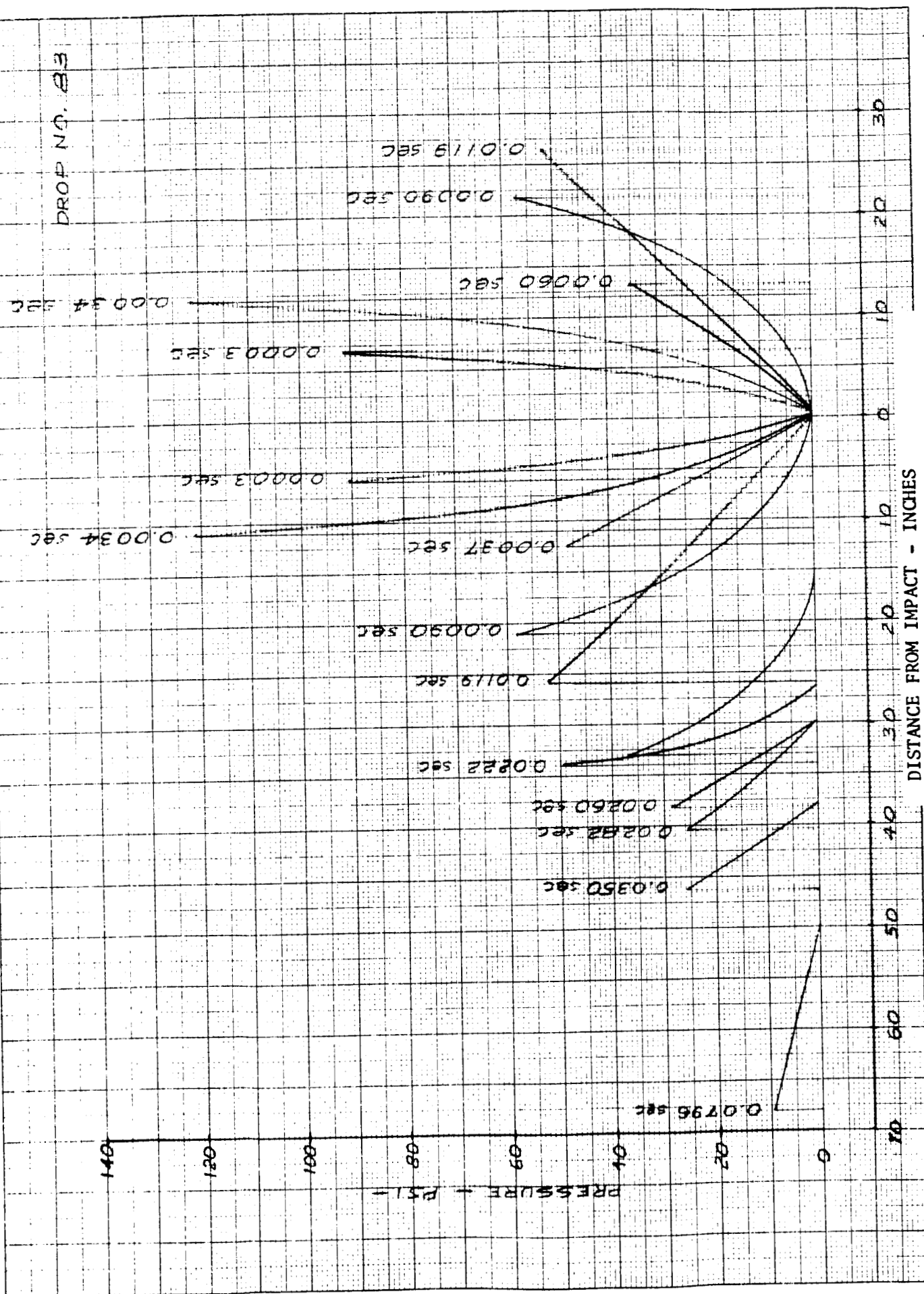Figure 6. Typical Pressure Profiles for a Slanting Impact at Times t_1, t_2.

Figure 7.   Experimental Pressure Distributions for Full Scale Test, V_0= 9 fps.
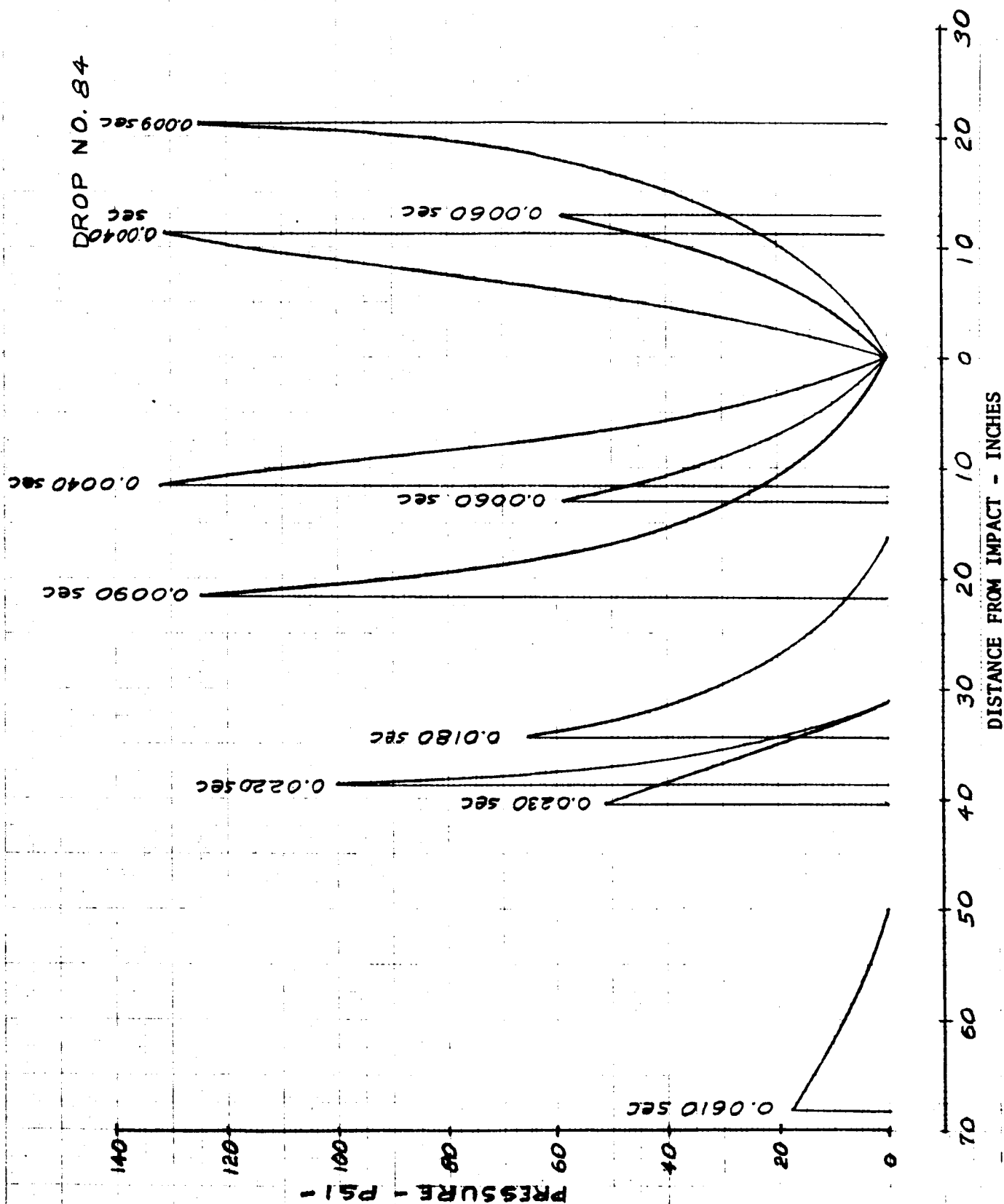
Figure 8. Experimental Pressure Distributions for Full Scale Test, V_o=16 fps.
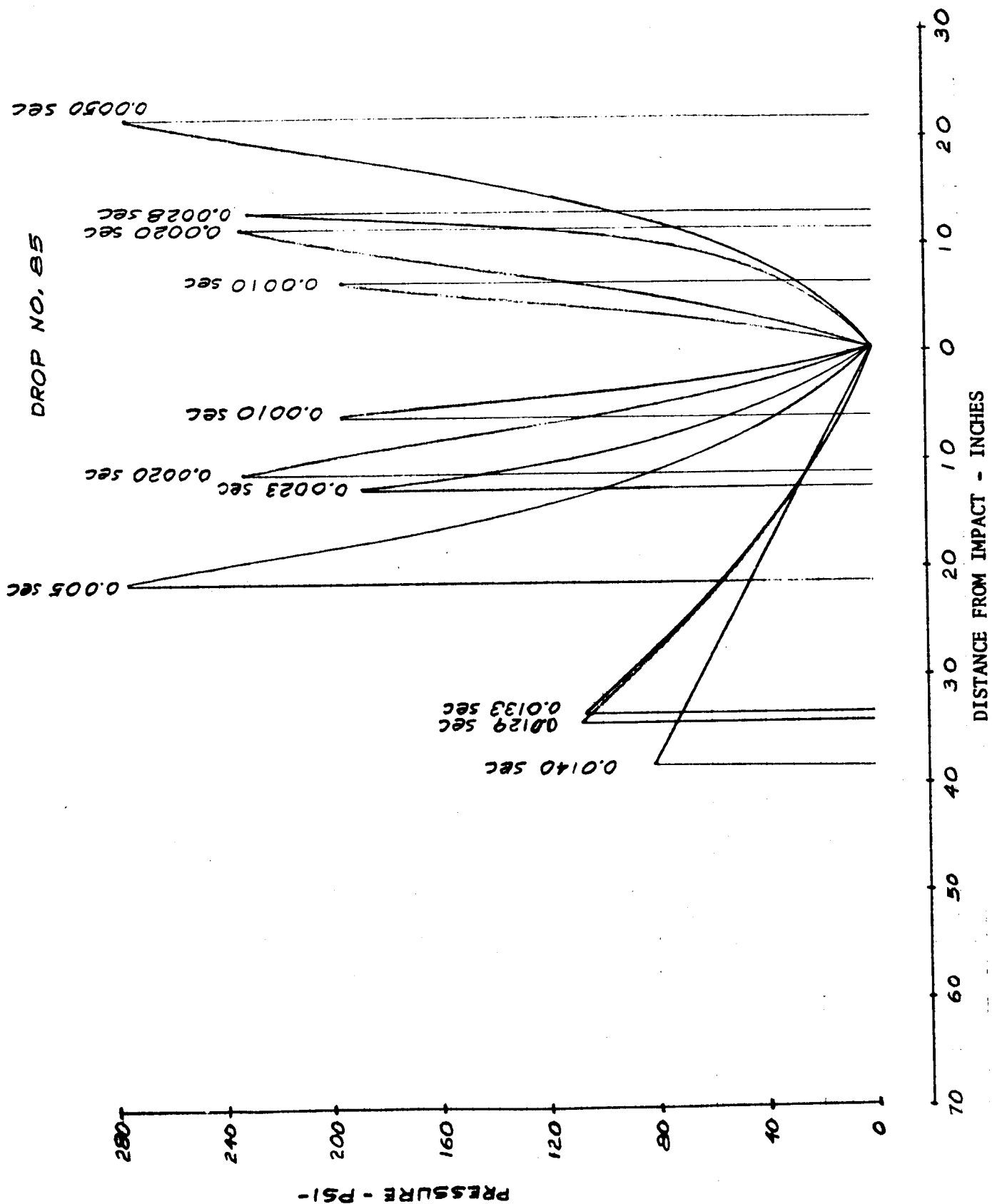
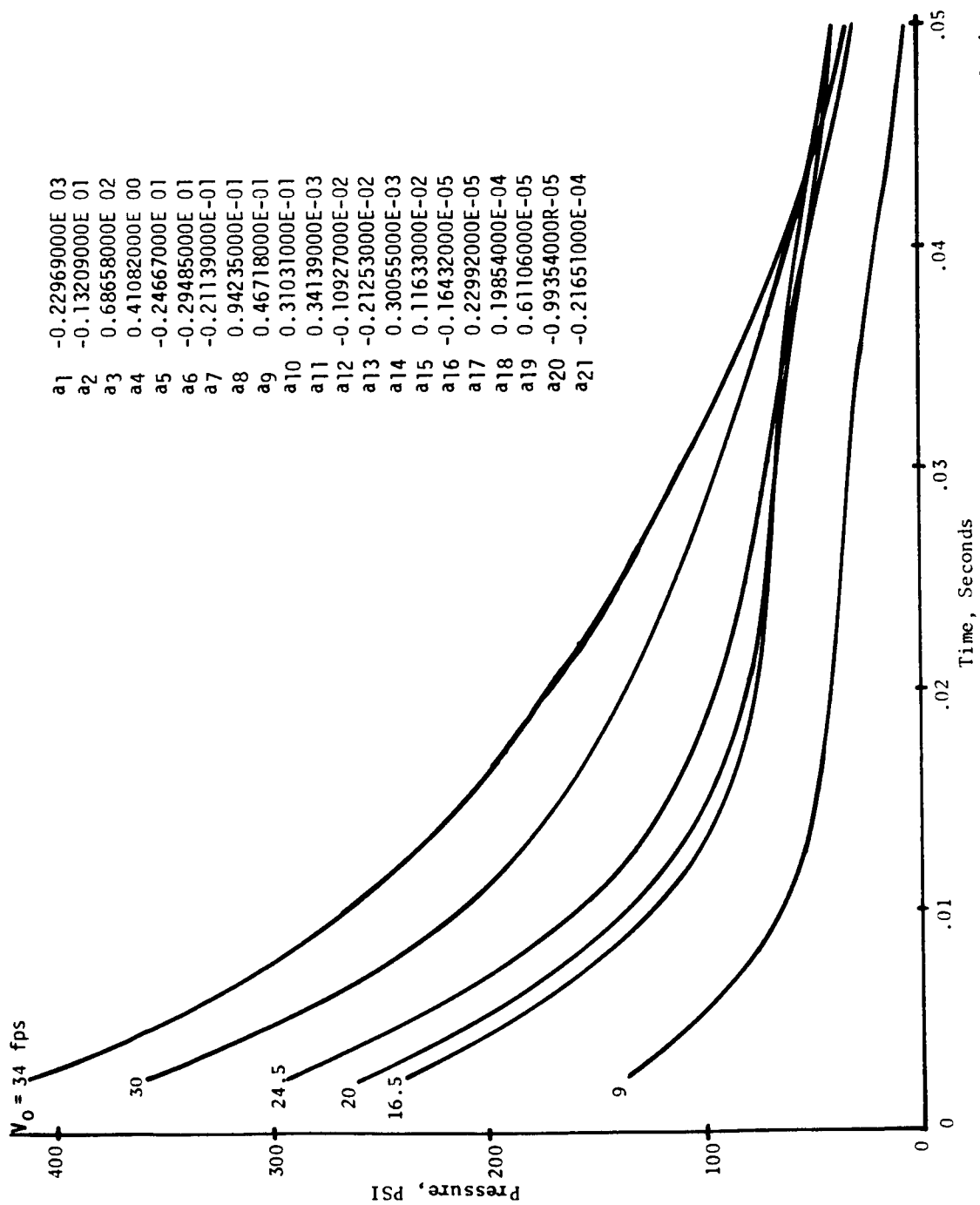Figure 9.   Experimental Pressure Distributions for Full Scale Test, V_0= 20 fps.

-28-
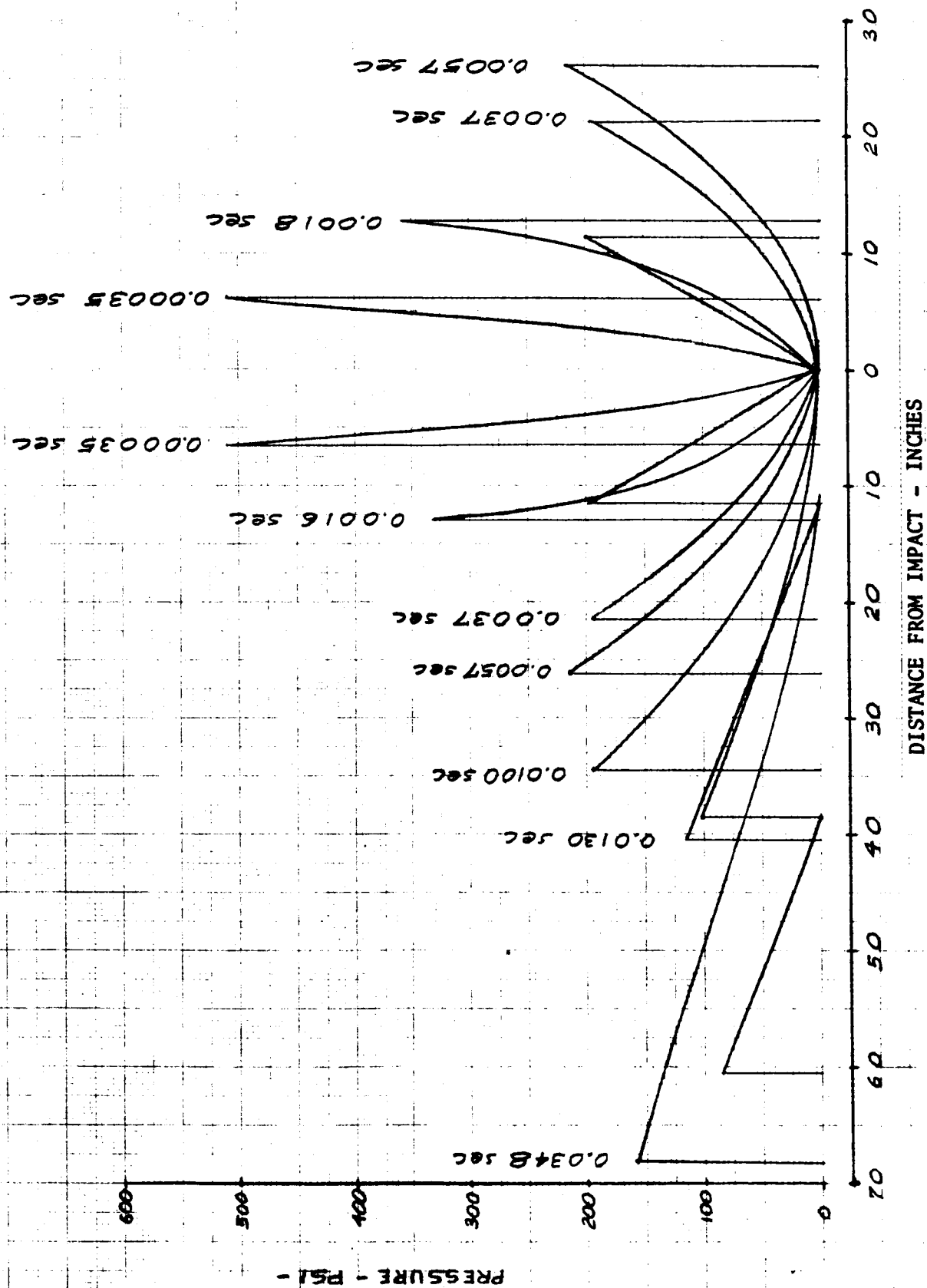
Figure 10. Experimental Pressure Distributions for Full Scale Test, V_o = 24.5 fps.
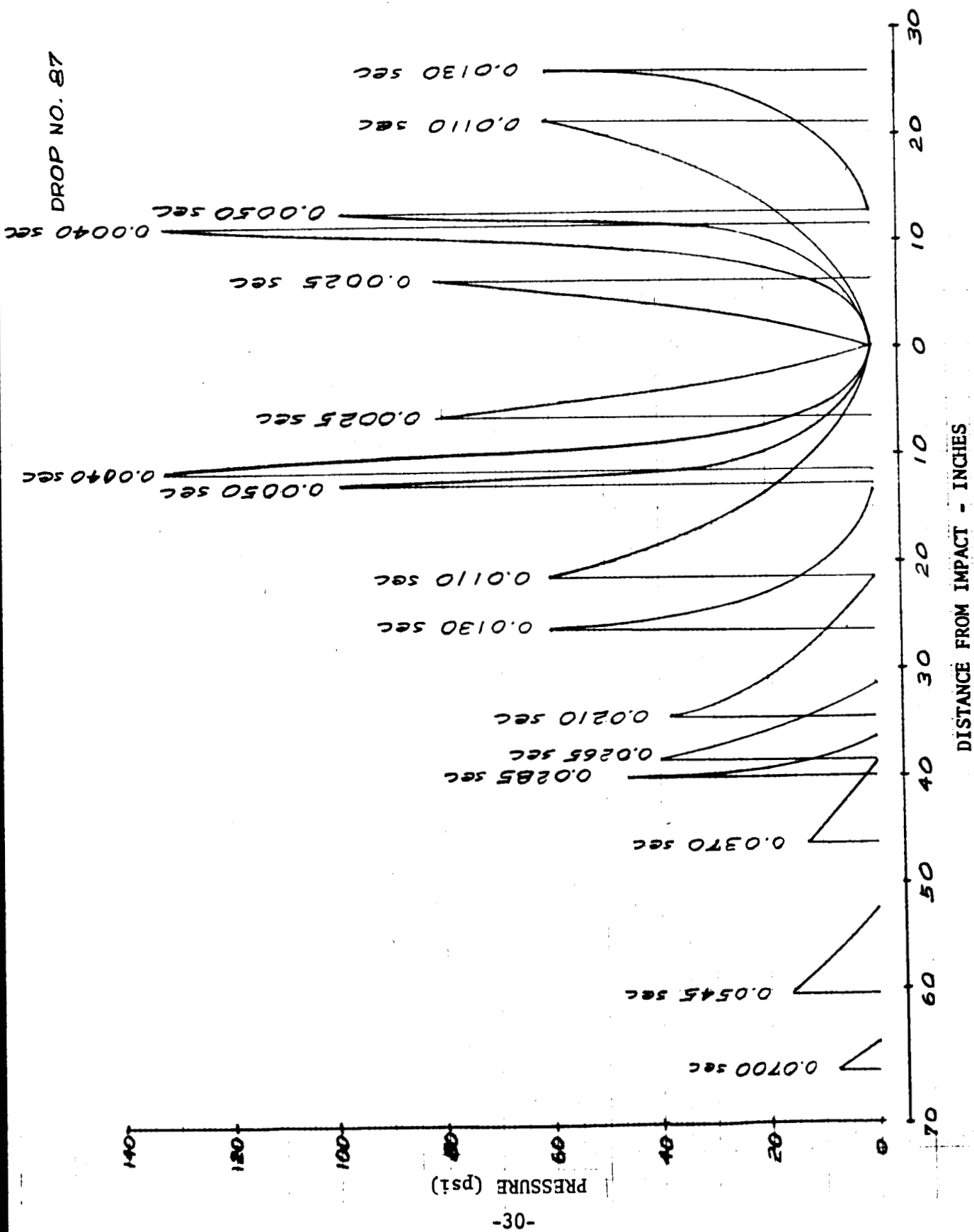
Figure 11. Experimental Pressure Distributions for Full Scale Test, V_o = 9 fps.

DROP NO. 87

0.0130 sec

0.0110 sec

0.0050 sec

0.0040 sec

0.0025 sec

0.0025 sec

0.0040 sec

0.0050 sec

0.0110 sec

0.0130 sec

0.0210 sec

0.0265 sec

0.0285 sec

0.0370 sec

0.0545 sec

0.0700 sec

DISTANCE FROM IMPACT - INCHES
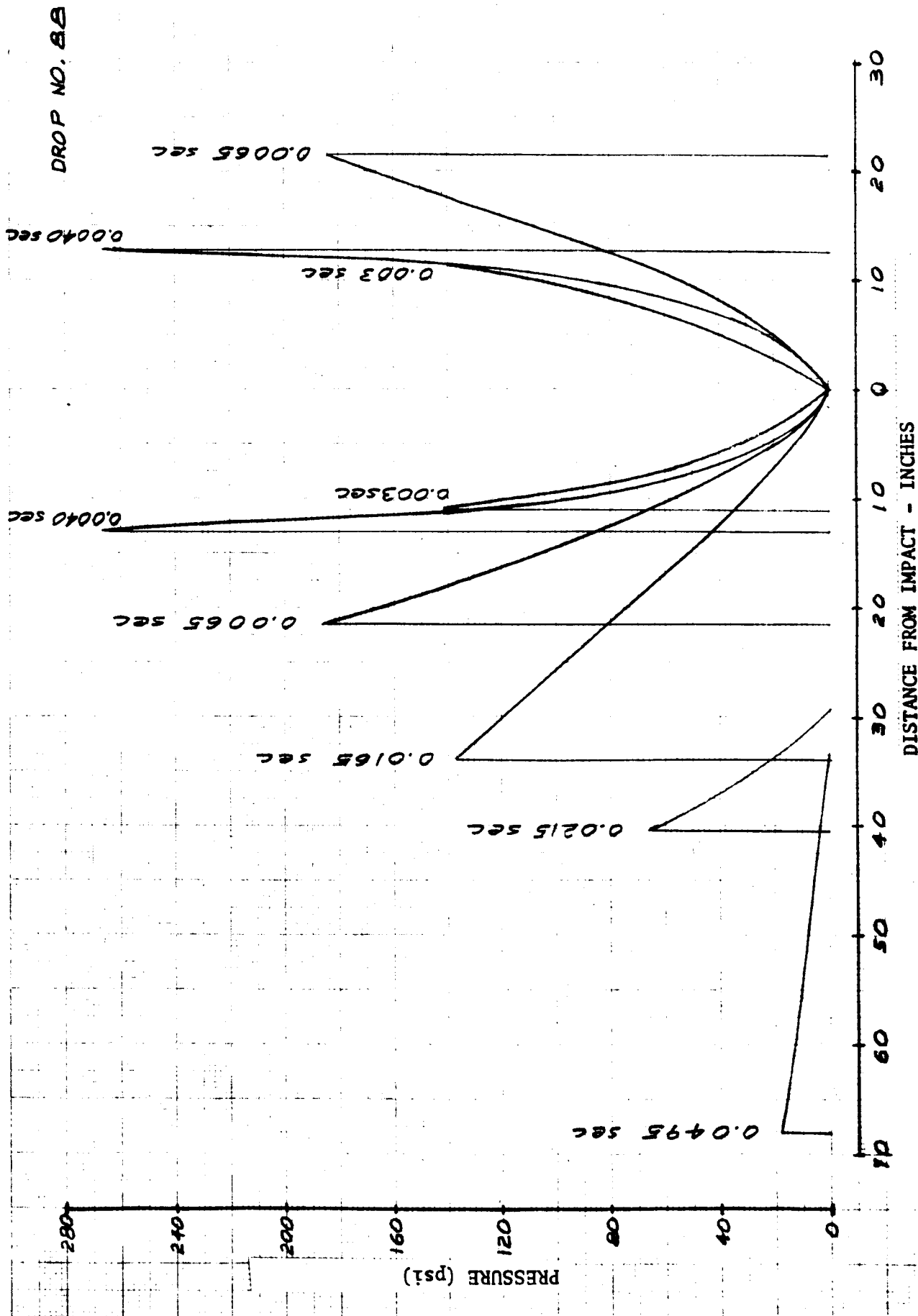
PRESSURE (psi)

Figure 12. Experimental Pressure Distributions for Full Scale Test, V_o= 17 fps.
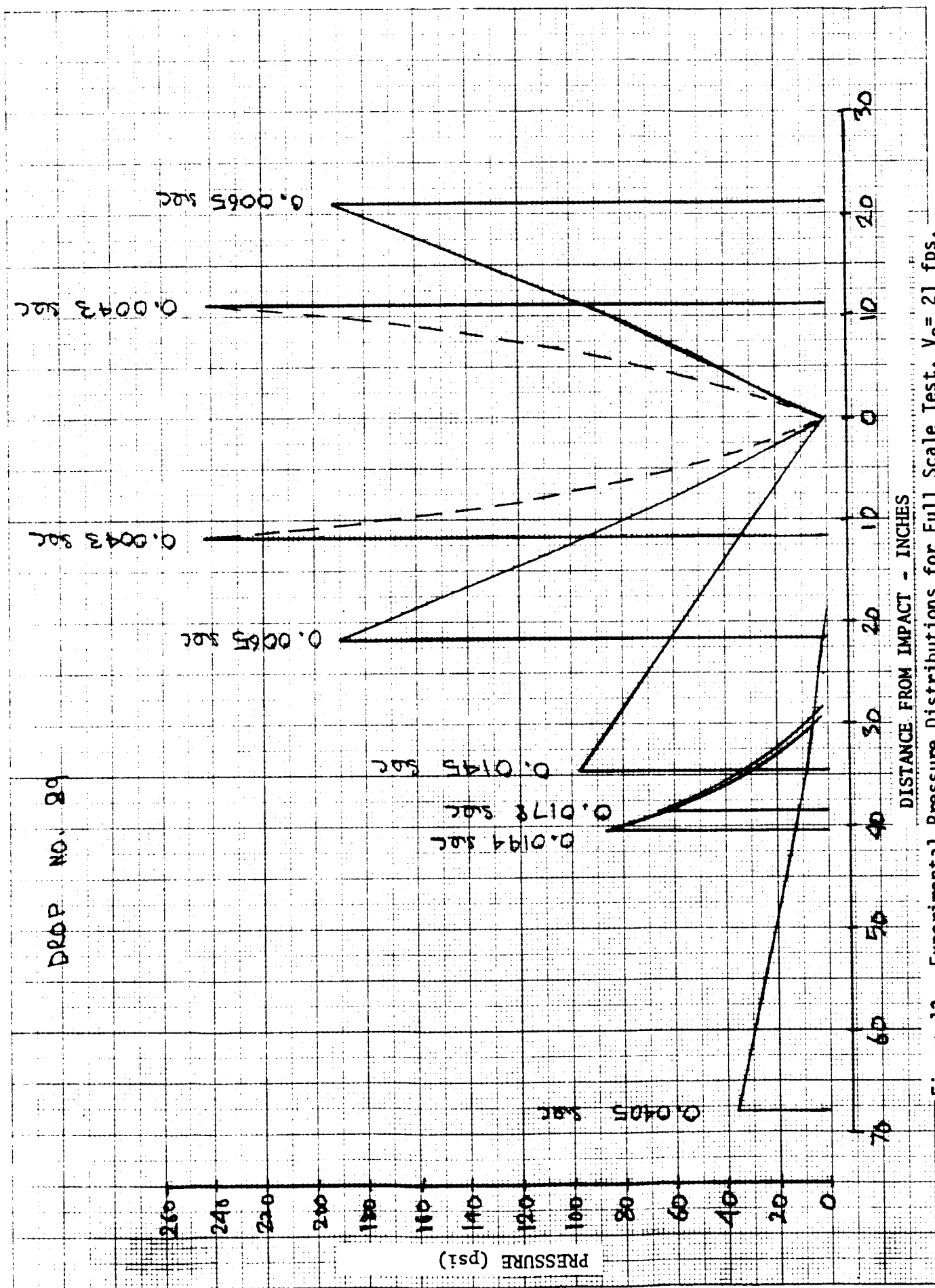
Figure 13. Experimental Pressure Distributions for Full Scale Test, V_o= 21 fps.

-32
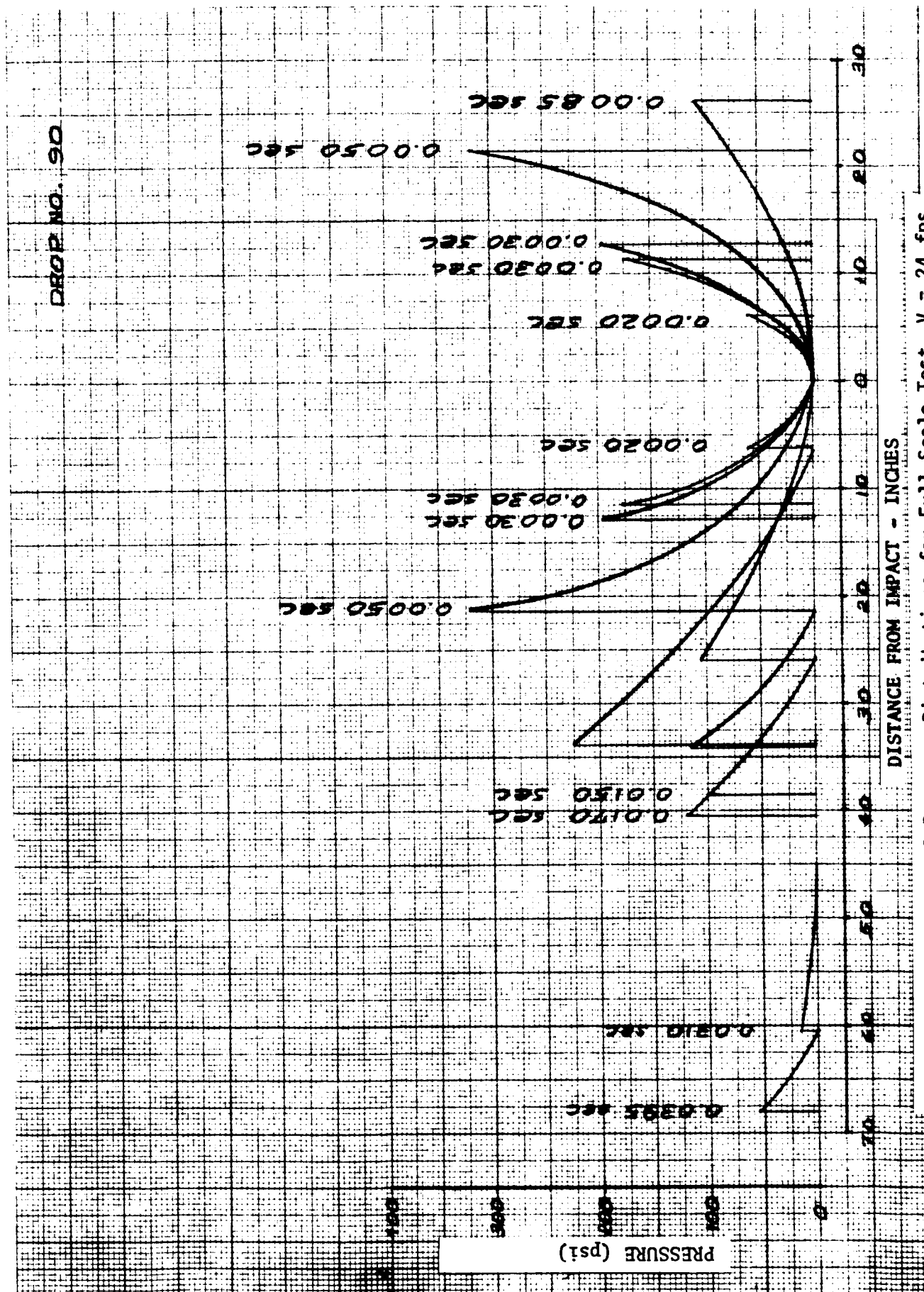
Figure 14. Experimental Pressure Distributions for Full Scale Test, V_0= 24 fps.

Figure 15. Empirical Relation for Maximum Pressure as a Function of Time and Initial Velocity.

a_1 -0.22969000E 03
a_2 -0.13209000E 01
a_3 0.68658000E 02
a_4 0.41082000E 00
a_5 -0.24667000E 01
a_6 -0.29485000E 01
a_7 -0.21139000E-01
a_8 0.94235000E-01
a_9 0.46718000E-01
a_{10} 0.31031000E-01
a_{11} 0.34139000E-03
a_{12} -0.10927000E-02
a_{13} -0.21253000E-02
a_{14} 0.30055000E-03
a_{15} 0.11633000E-02
a_{16} -0.16432000E-05
a_{17} 0.22992000E-05
a_{18} 0.19854000E-04
a_{19} 0.61106000E-05
a_{20} -0.99354000R-05
a_{21} -0.21651000E-04

V_o = 34 fps

30

24.5

20

16.5

9

Time, Seconds

Pressure, PSI

-34-

Figure 16. Empirical Relation for Maximum Pressure, $V_0 = 9$ fps.
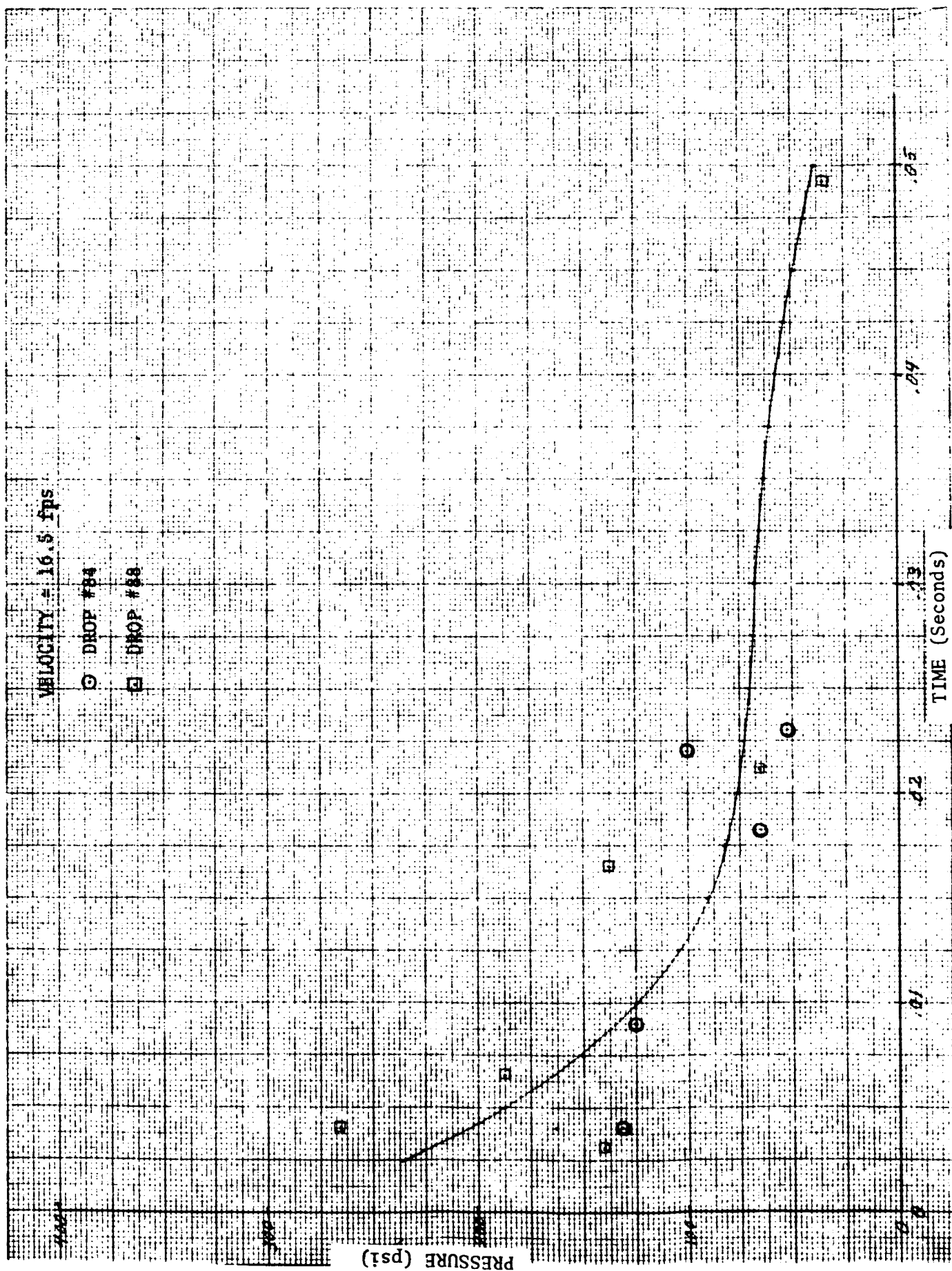
Figure 17. Empirical Relation for Maximum Pressure, V_0= 16.5 fps.
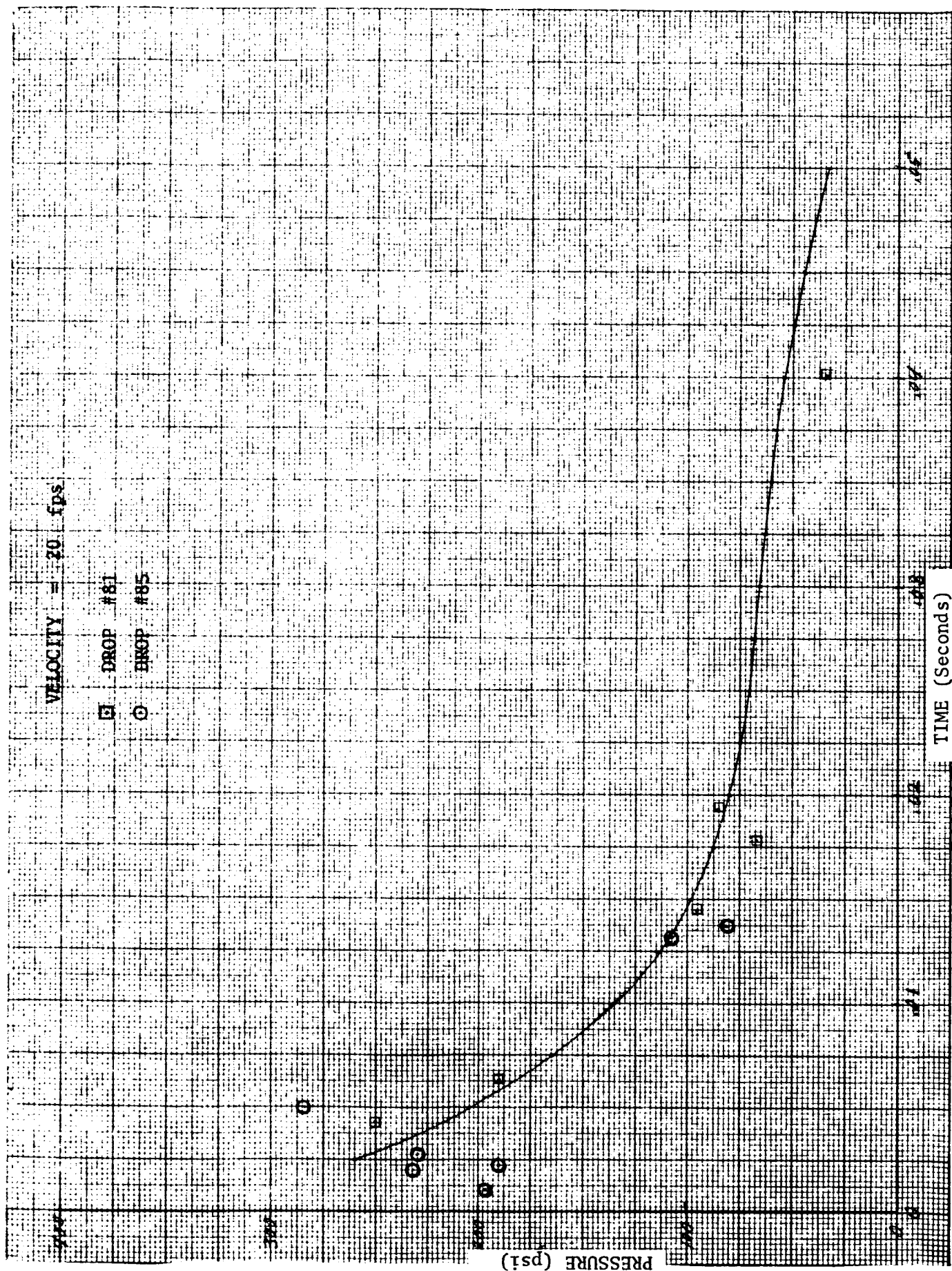
Figure 18. Empirical Relation for Maximum Pressure, $V_o = 20$ fps.

-37-
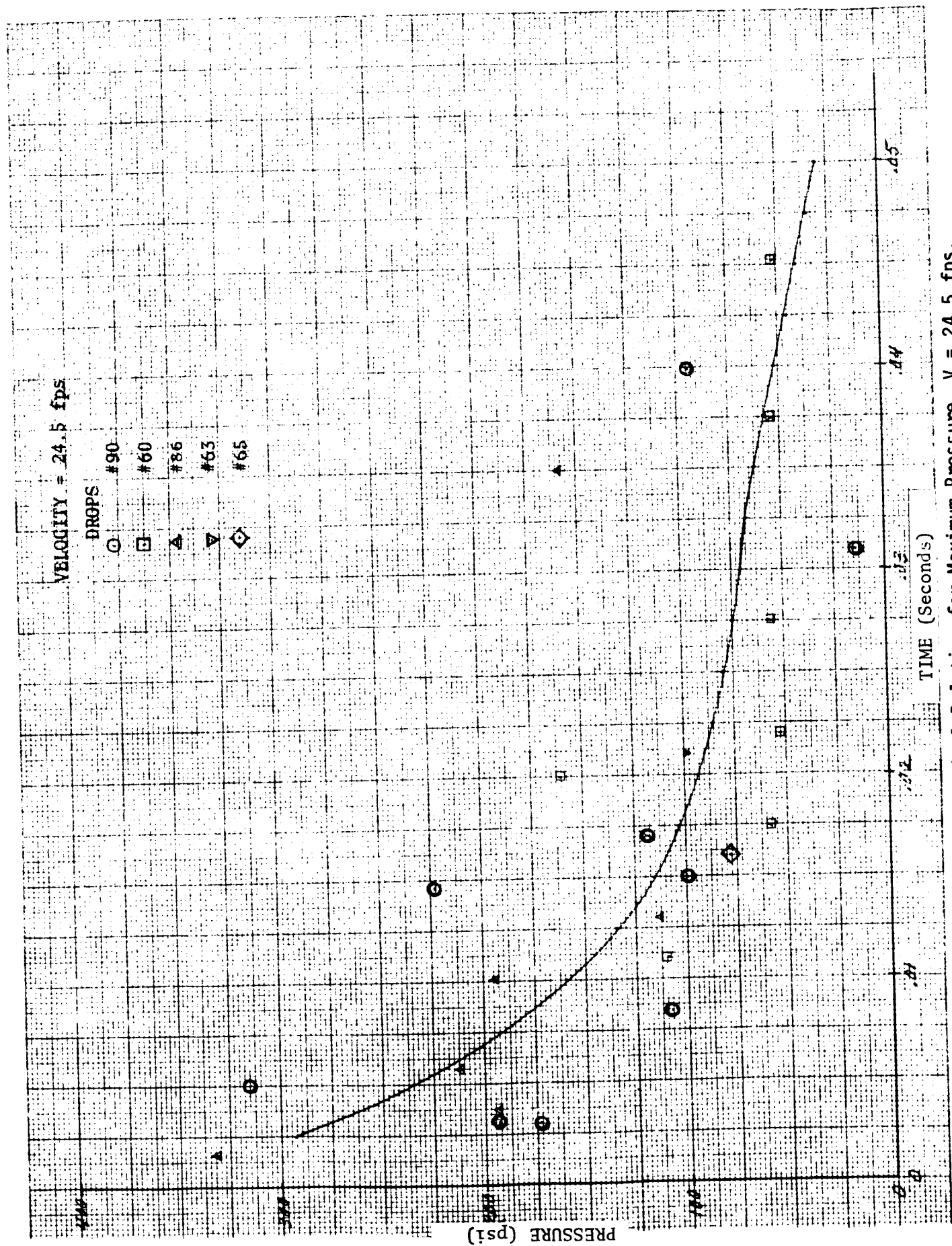
Figure 19. Empirical Relation for Maximum Pressure, V_o= 24.5 fps.

-38-

Figure 20. Empirical Relation for Maximum Pressure, $V_0 = 30$ fps.
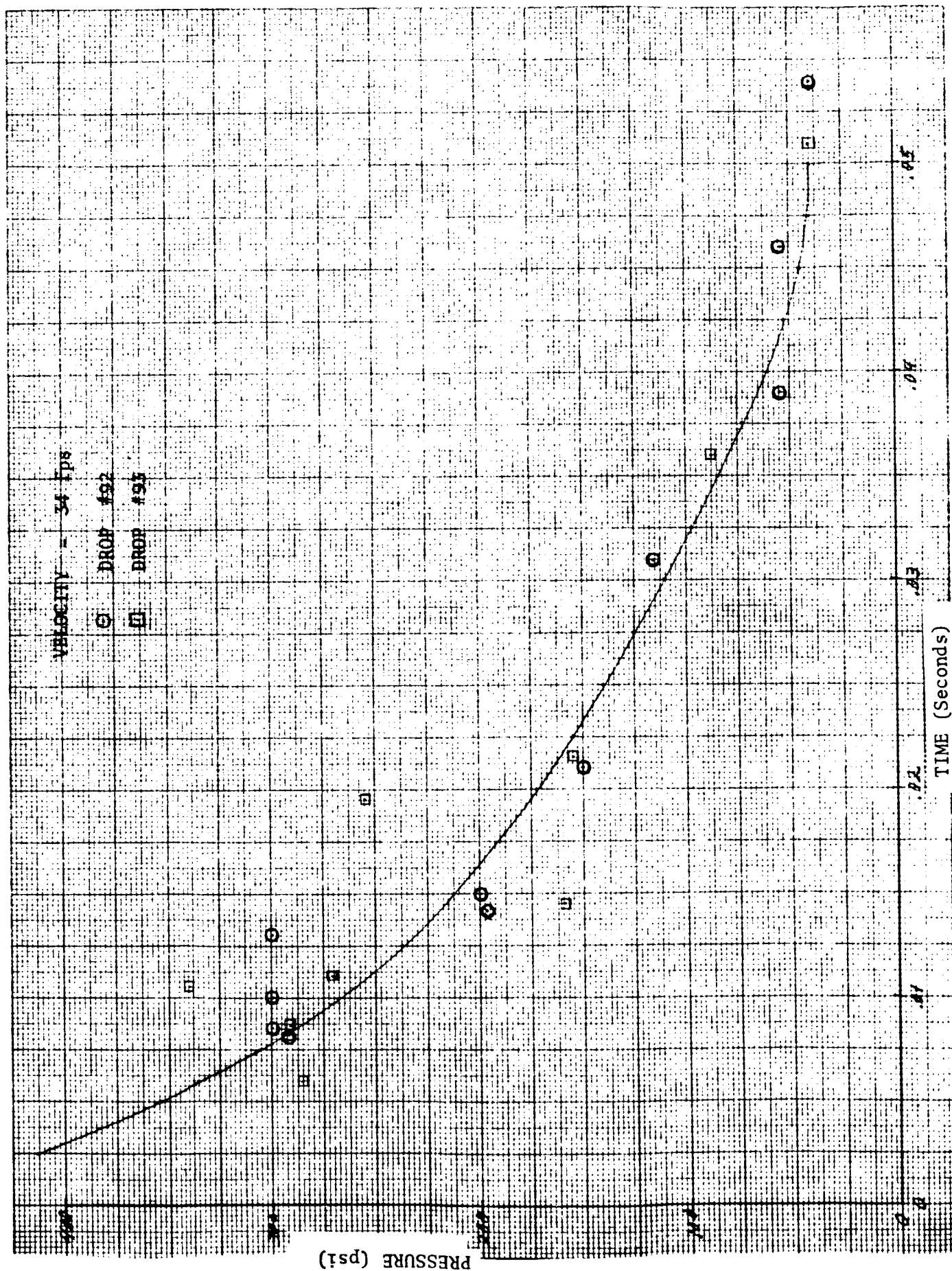
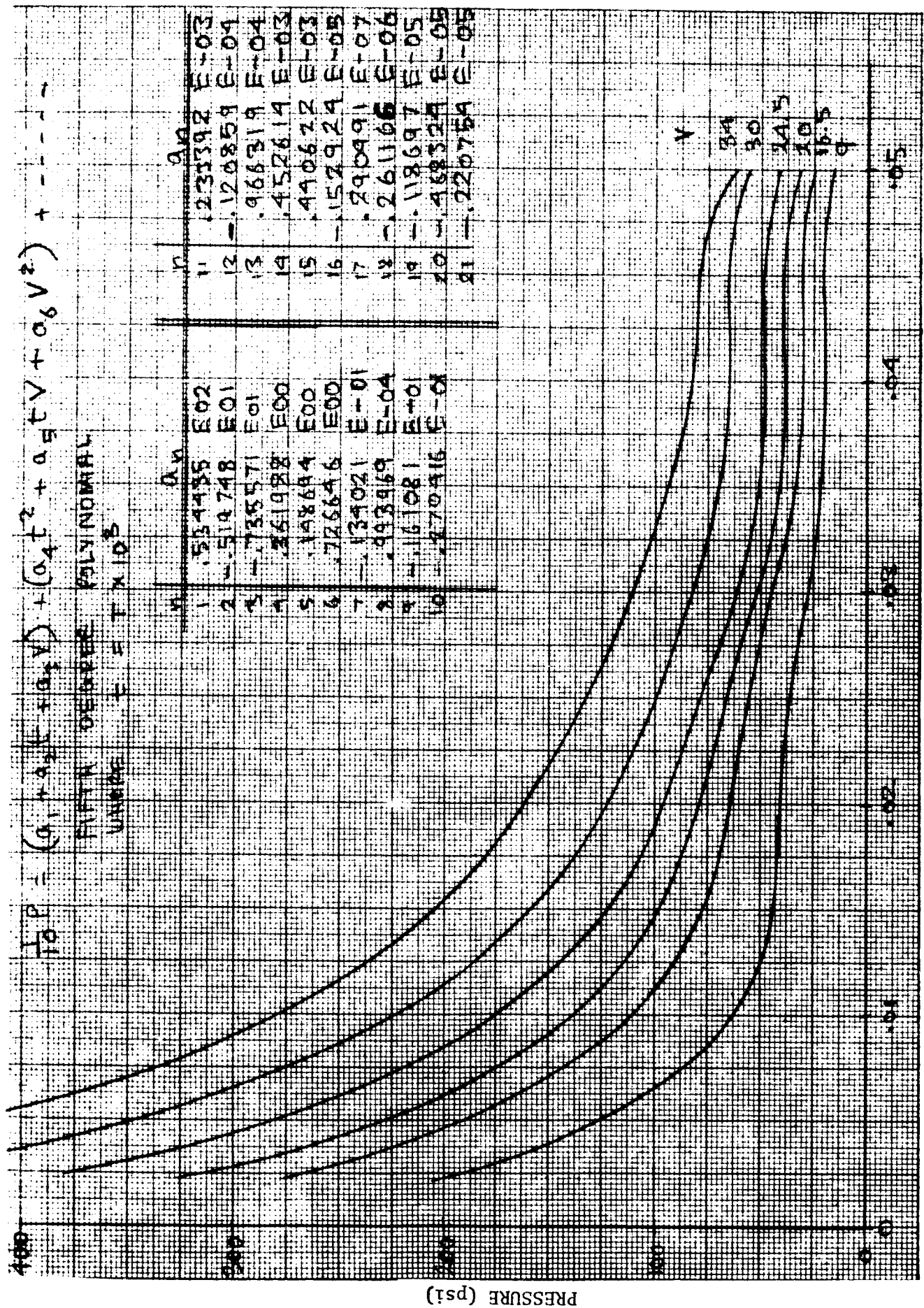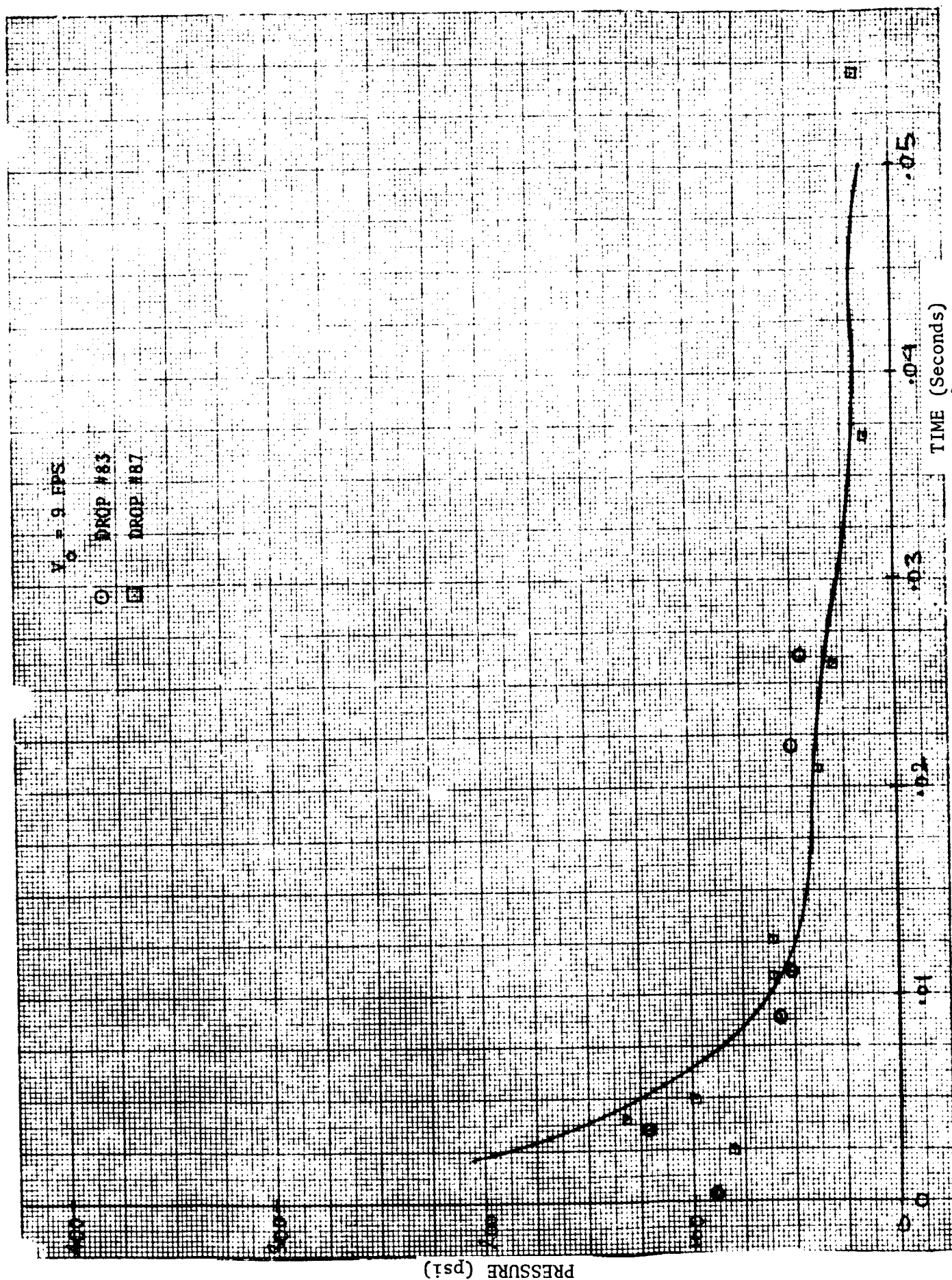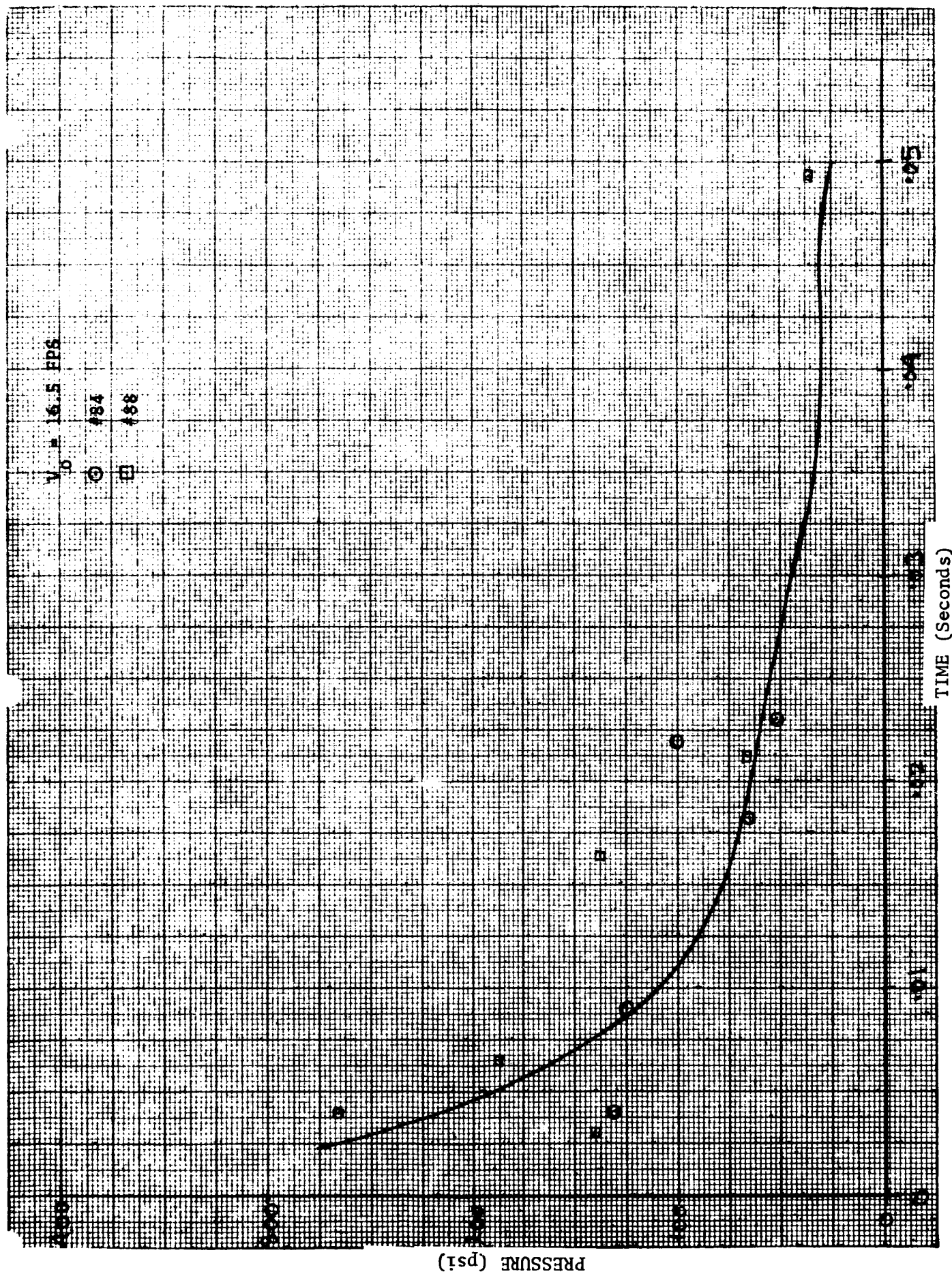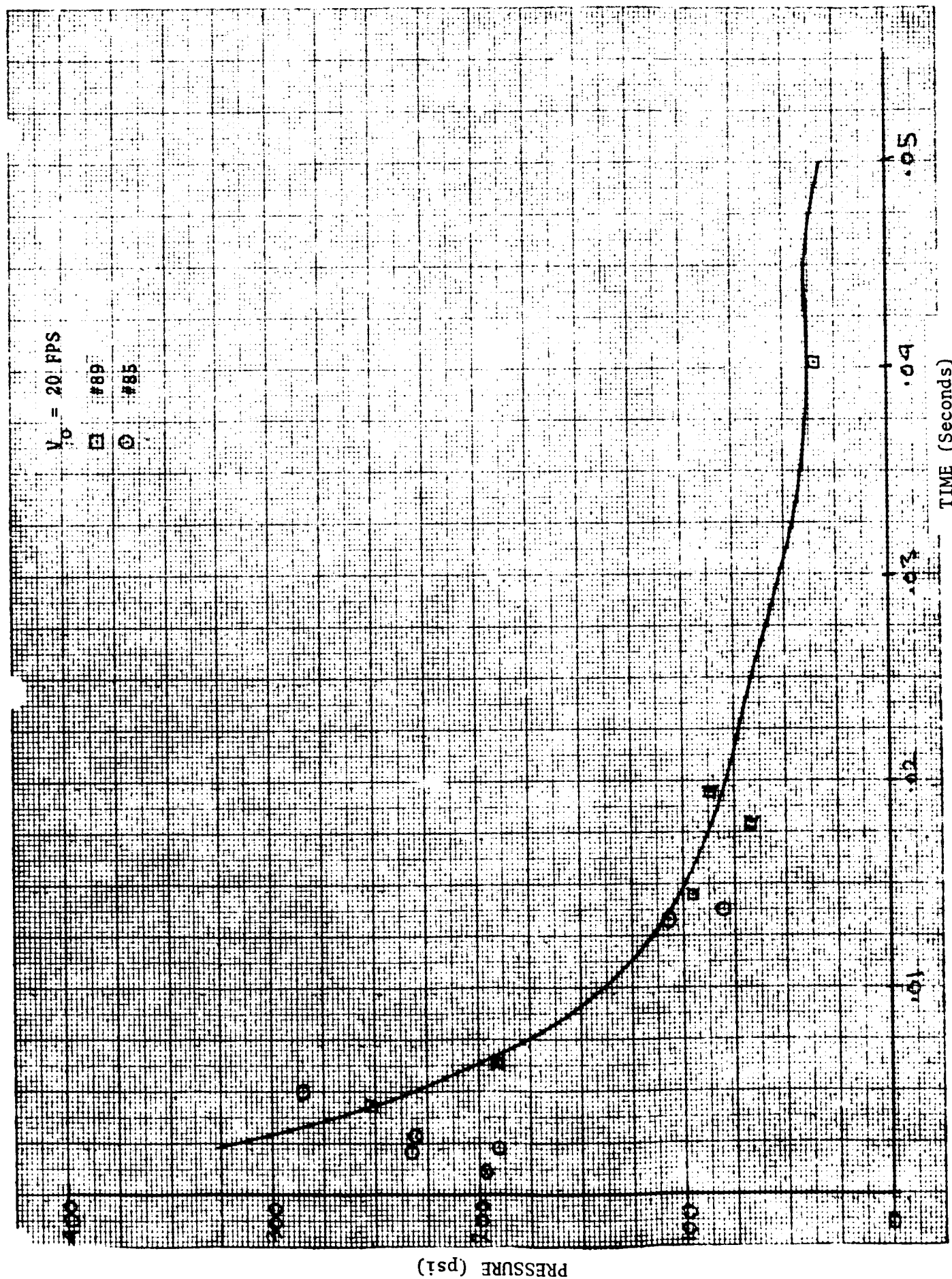Figure 21. Empirical Relation for Maximum Pressure V_0 = 34 fps.

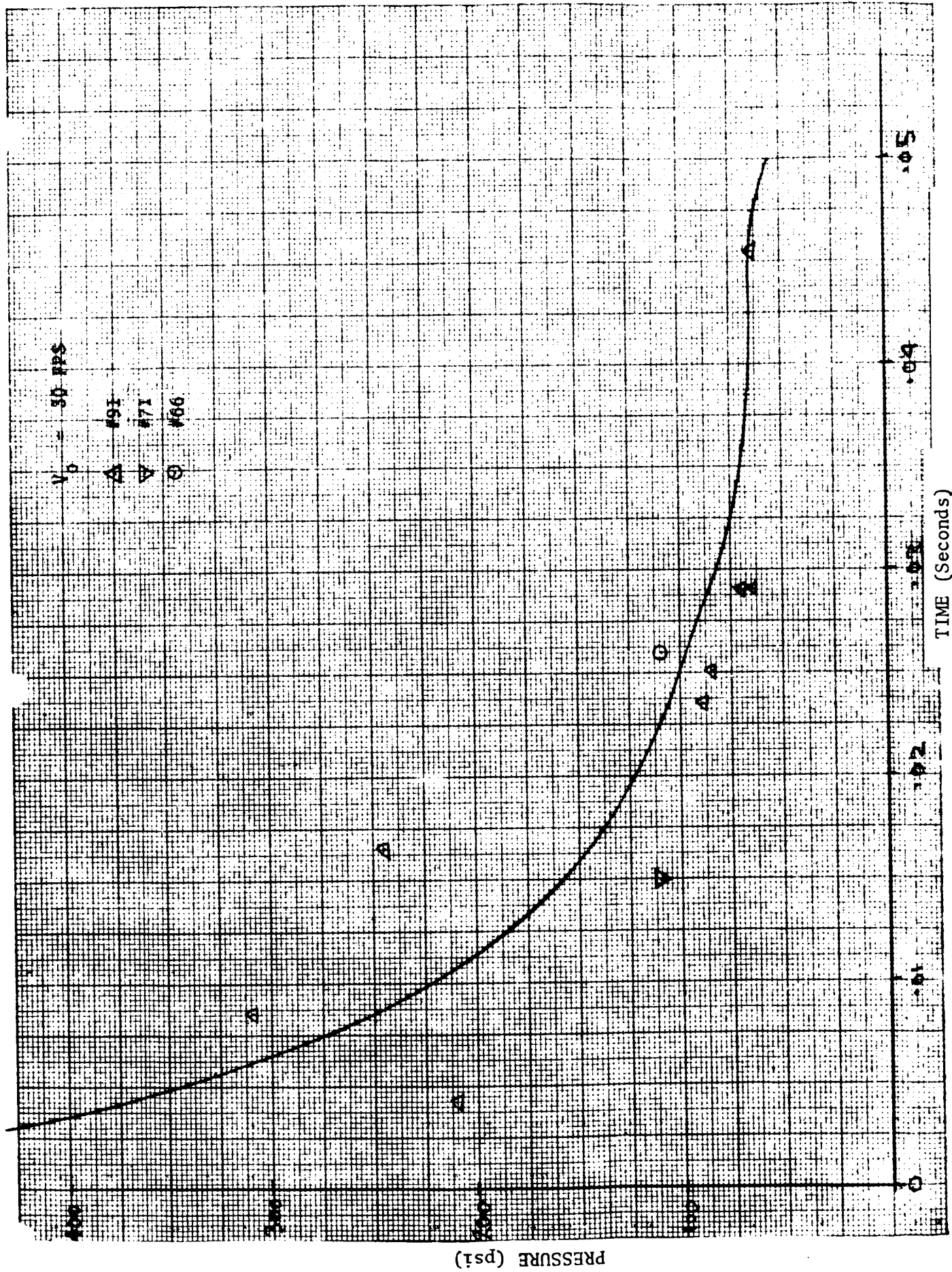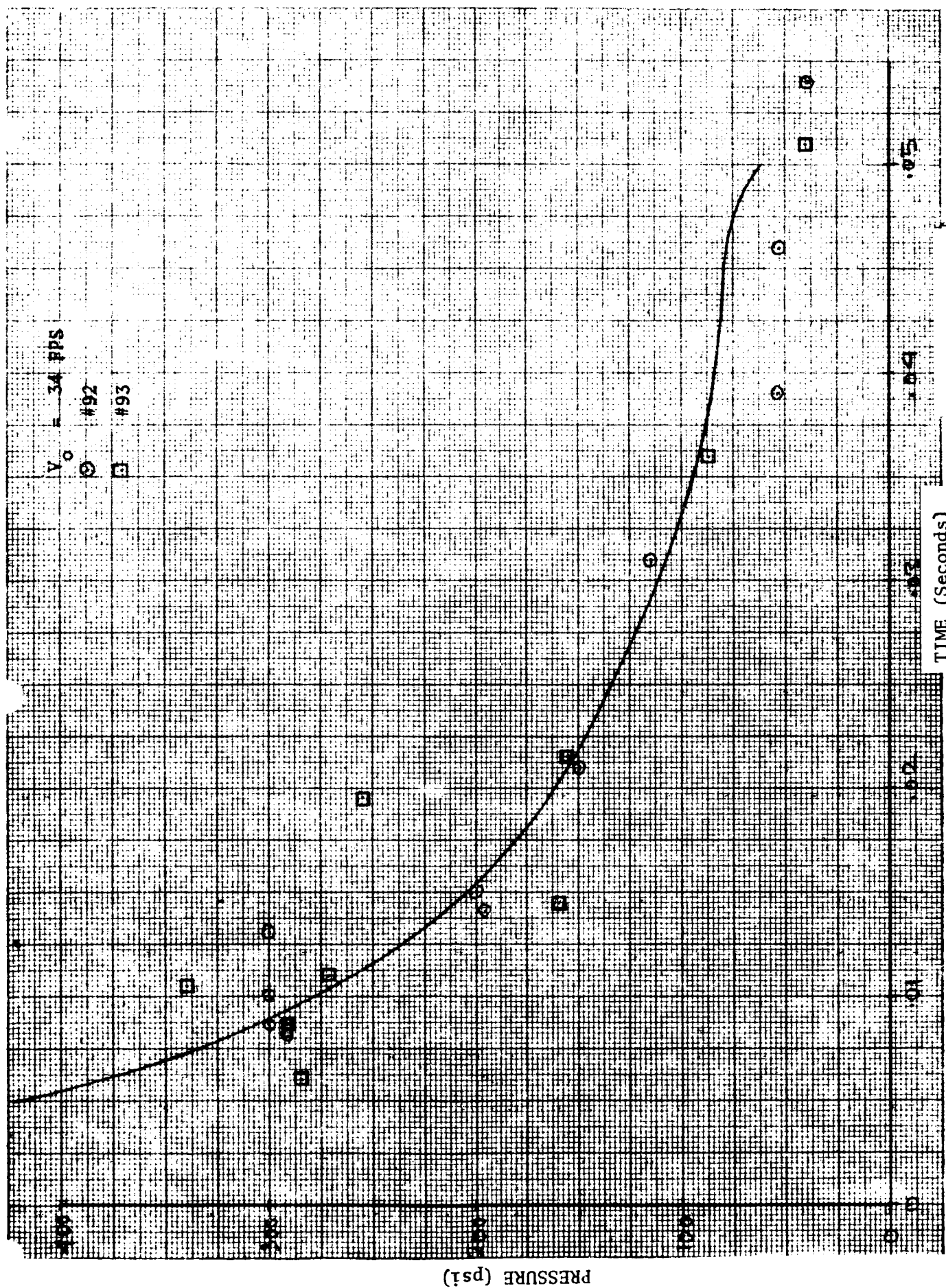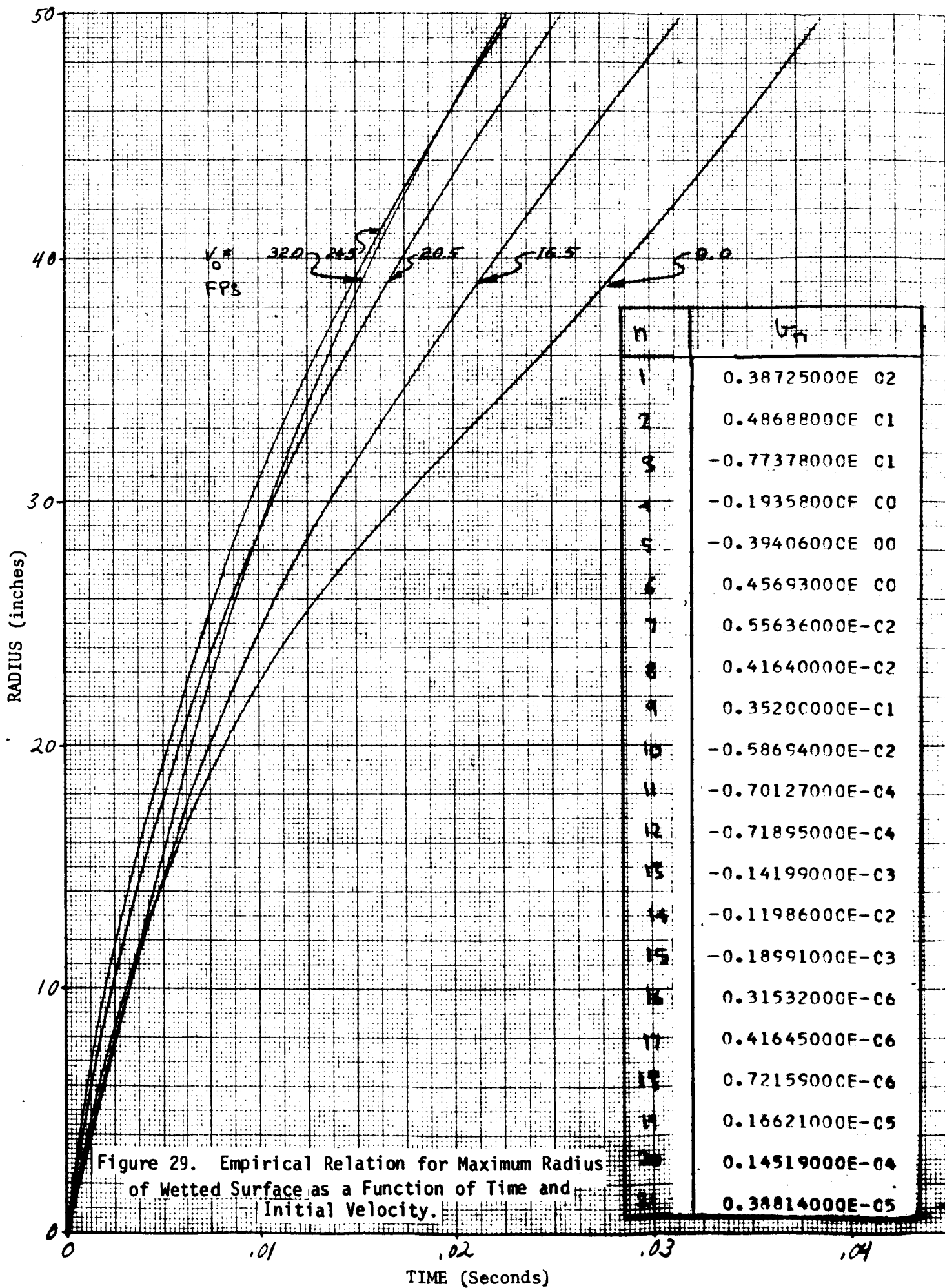$$P = (a_1 + a_2 t + a_3 V) + (a_4 t^2 + a_9 tV + a_6 V^2) + \cdots$$

FIFTH DEGREE POLYNOMIAL

UNITS: $n = t \times 10^5$

n	a_n	
1	.554455	E 02
2	-.514748	E 01
3	-.735571	E 01
4	.361988	E 00
5	.148694	E 00
6	.726646	E 00
7	-.134021	E-01
8	-.443969	E-04
9	-.116081	E+01
10	.270916	E-04

n	a_n	
11	.233392	E-03
12	-.120859	E+01
13	.966319	E-04
14	.452614	E-03
15	.440672	E-03
16	-.152924	E-05
17	.290991	E-07
18	-.261166	E-06
19	-.118697	E-05
20	-.468324	E-05
21	-.220754	E-05

V
34
30
24.5
20
16.5
9

PRESSURE (psi)

TIME (Seconds)

Figure 22. Alternate Empirical Relation for Maximum Pressure.

Figure 23. Empirical Relation for Maximum Pressure, V_0 = 9 fps.

-42-

Figure 24. Empirical Relation for Maximum Pressure, V_0 = 16.5 fps.

Figure 25. Empirical Relation for Maximum Pressure, $V_0 = 20$ fps.

-44-
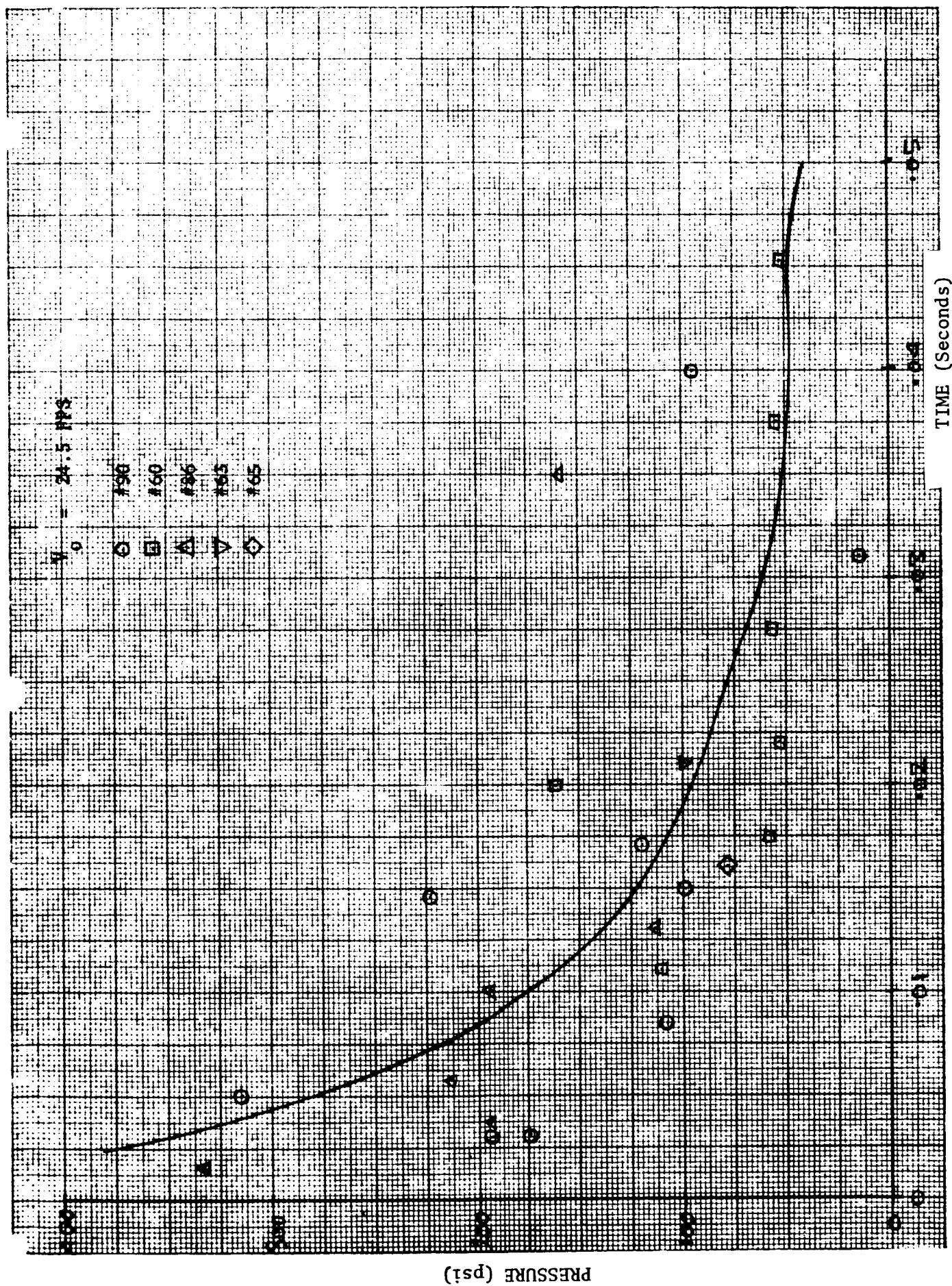
Figure 26. Empirical Relation for Maximum Pressure, V_0 = 24.5 fps.

PRESSURE (psi)
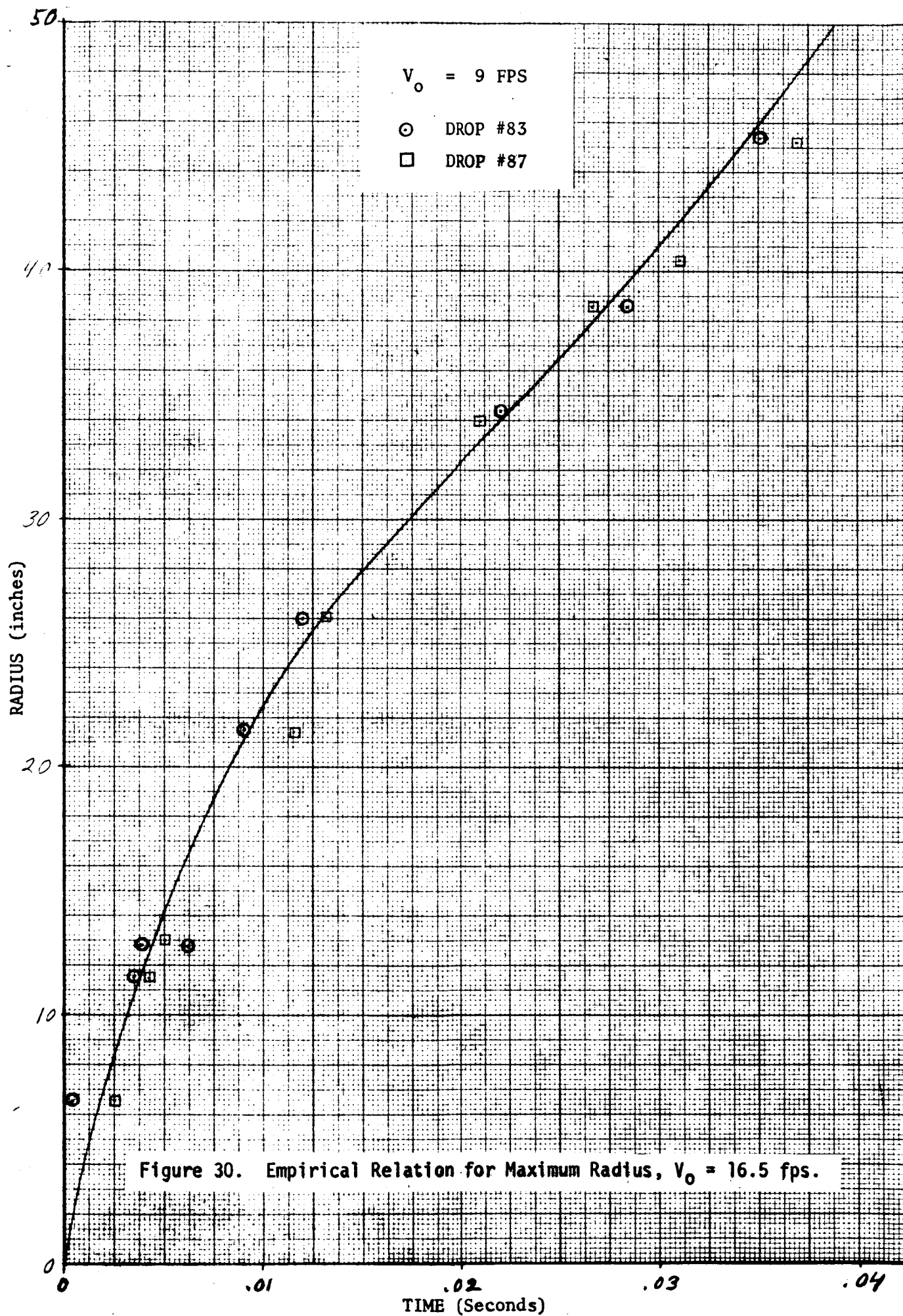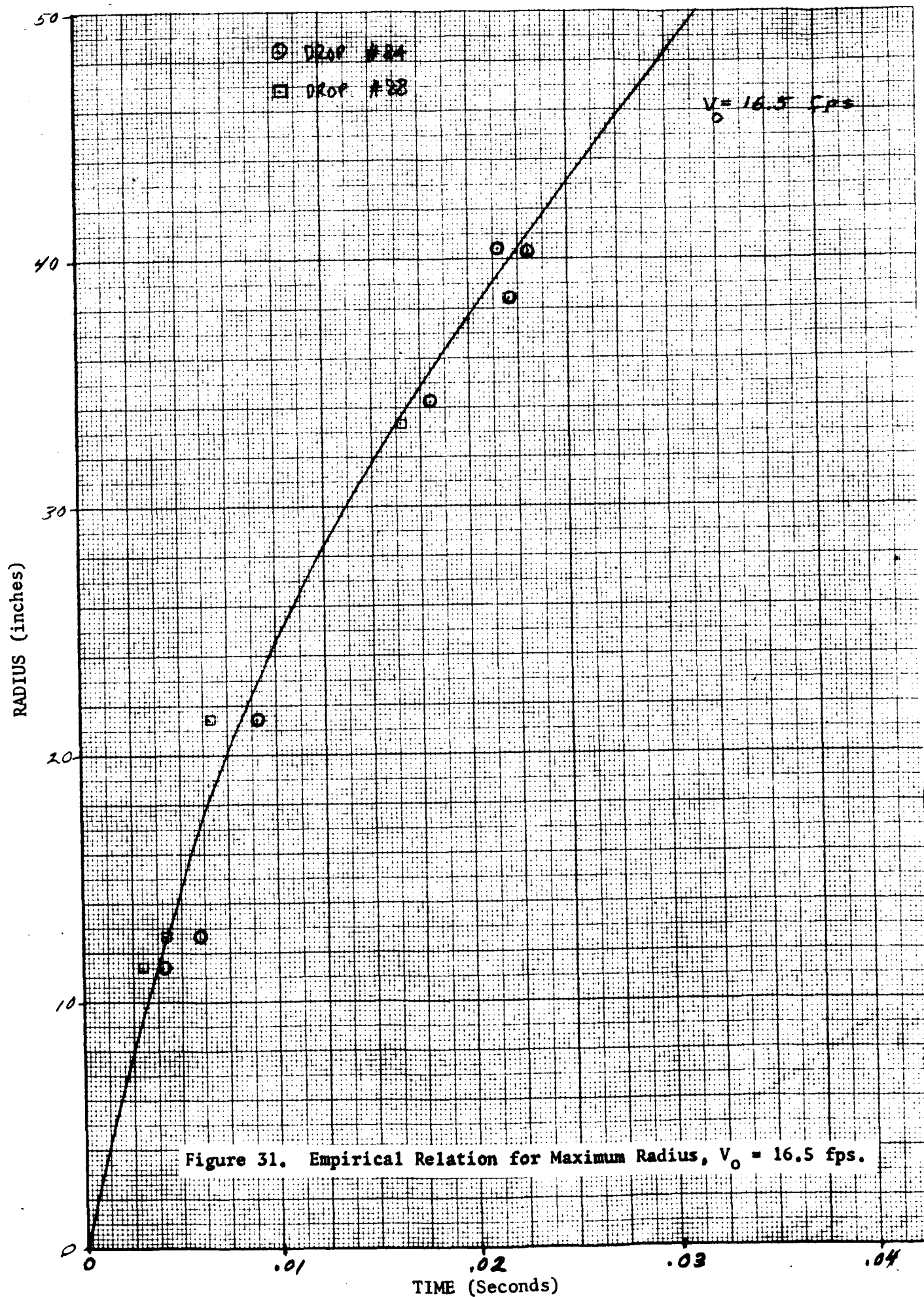
TIME (Seconds)

$V_0 = 30$ FPS

△ #91
▽ #71
⊖ #66

-46-

Figure 28. Empirical Relation for Maximum Pressure, V_0 = 34 fps.

-47-

$V_o =$ 32.0   26.5   20.5   16.5   0.0   FPS

RADIUS (inches)

n	V_n
1	0.38725000E 02
2	0.48688000E 01
3	-0.77378000E 01
4	-0.19358000E 00
5	-0.39406000E 00
6	0.45693000E 00
7	0.55636000E-02
8	0.41640000E-02
9	0.35200000E-01
10	-0.58694000E-02
11	-0.70127000E-04
12	-0.71895000E-04
13	-0.14199000E-03
14	-0.11986000E-02
15	-0.18991000E-03
16	0.31532000E-06
17	0.41645000E-06
18	0.72159000E-06
19	0.16621000E-05
20	0.14519000E-04
21	0.38814000E-05

Figure 29.   Empirical Relation for Maximum Radius of Wetted Surface as a Function of Time and Initial Velocity.

TIME (Seconds)

Figure 30. Empirical Relation for Maximum Radius, V_o = 16.5 fps.
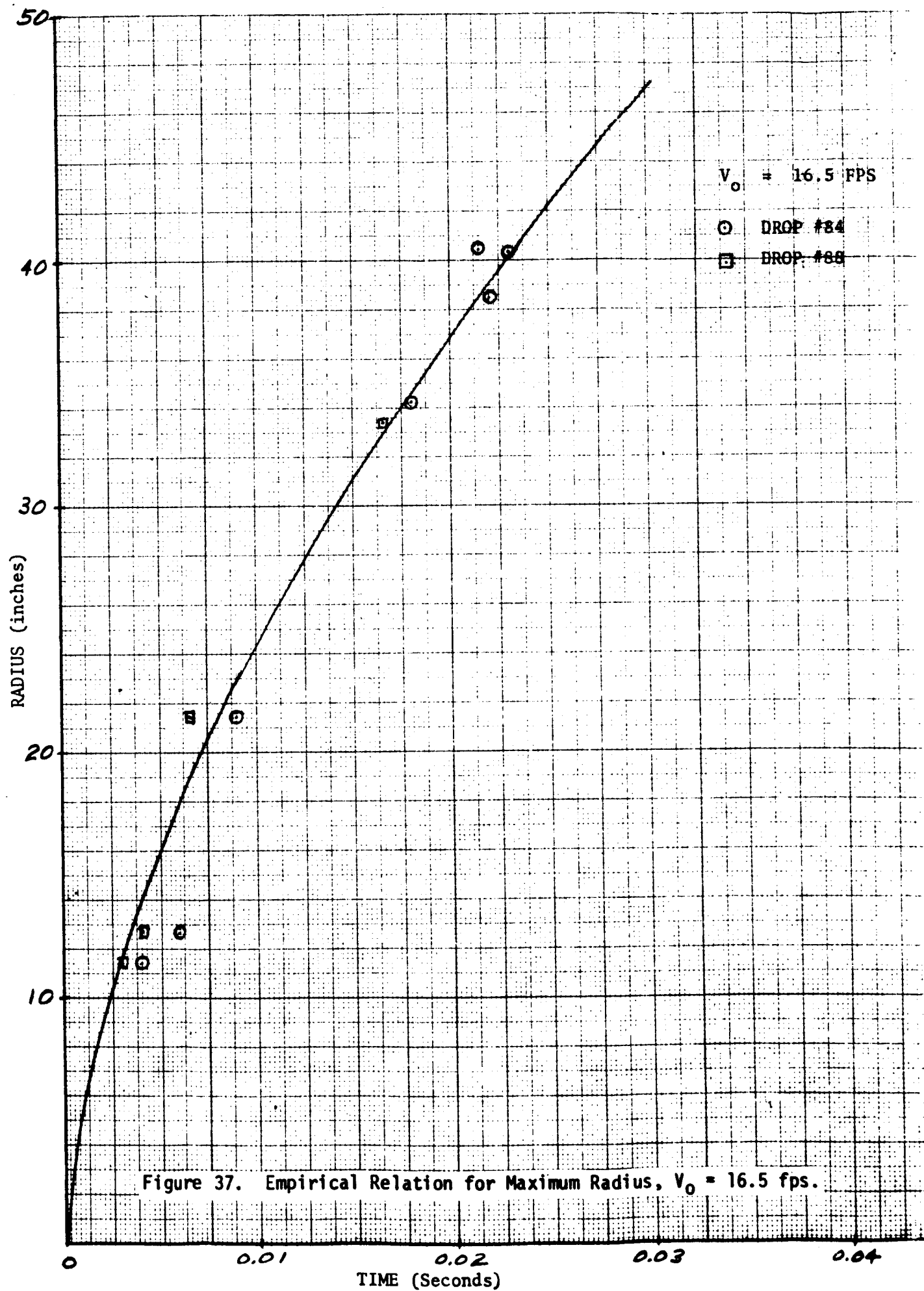
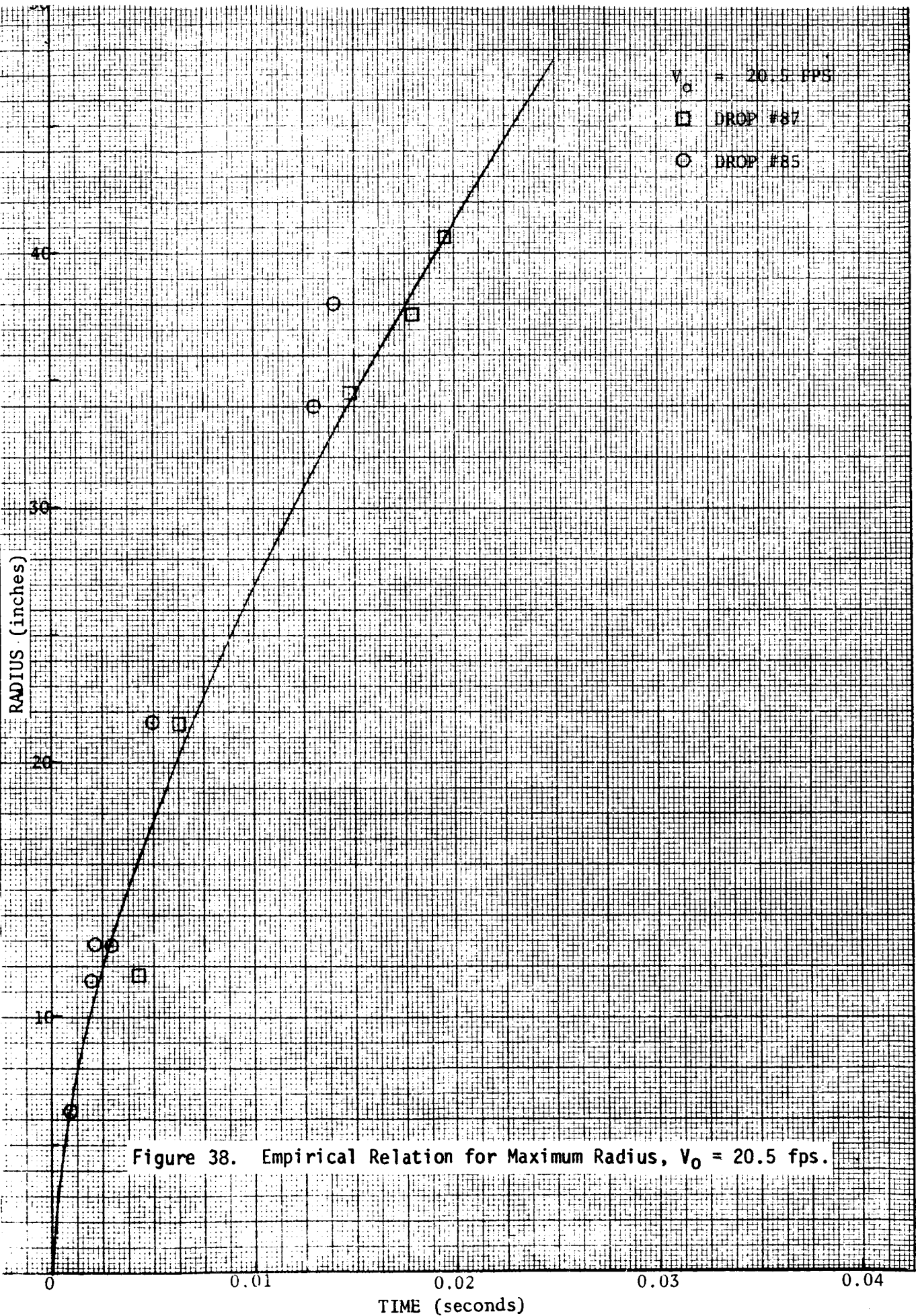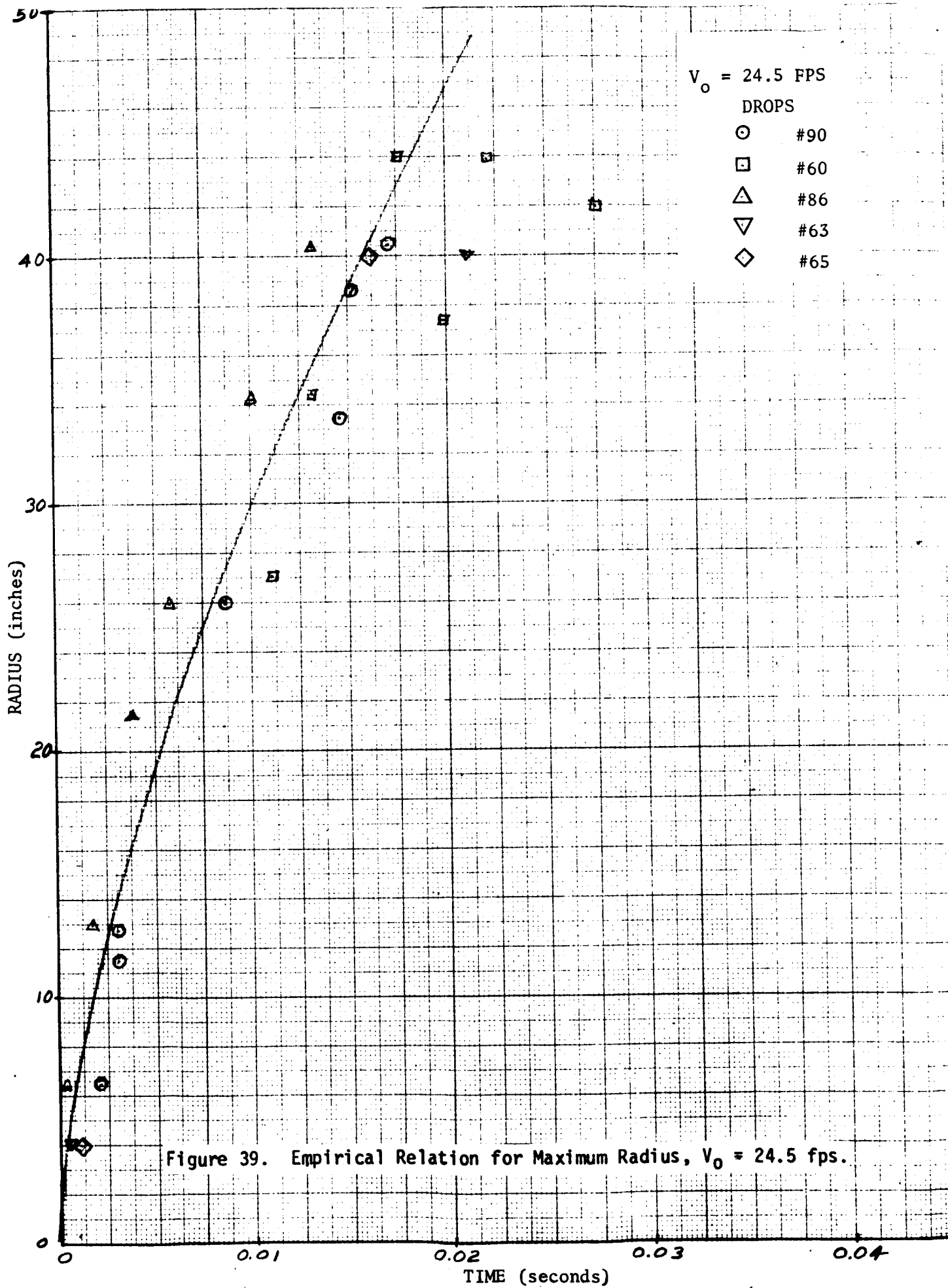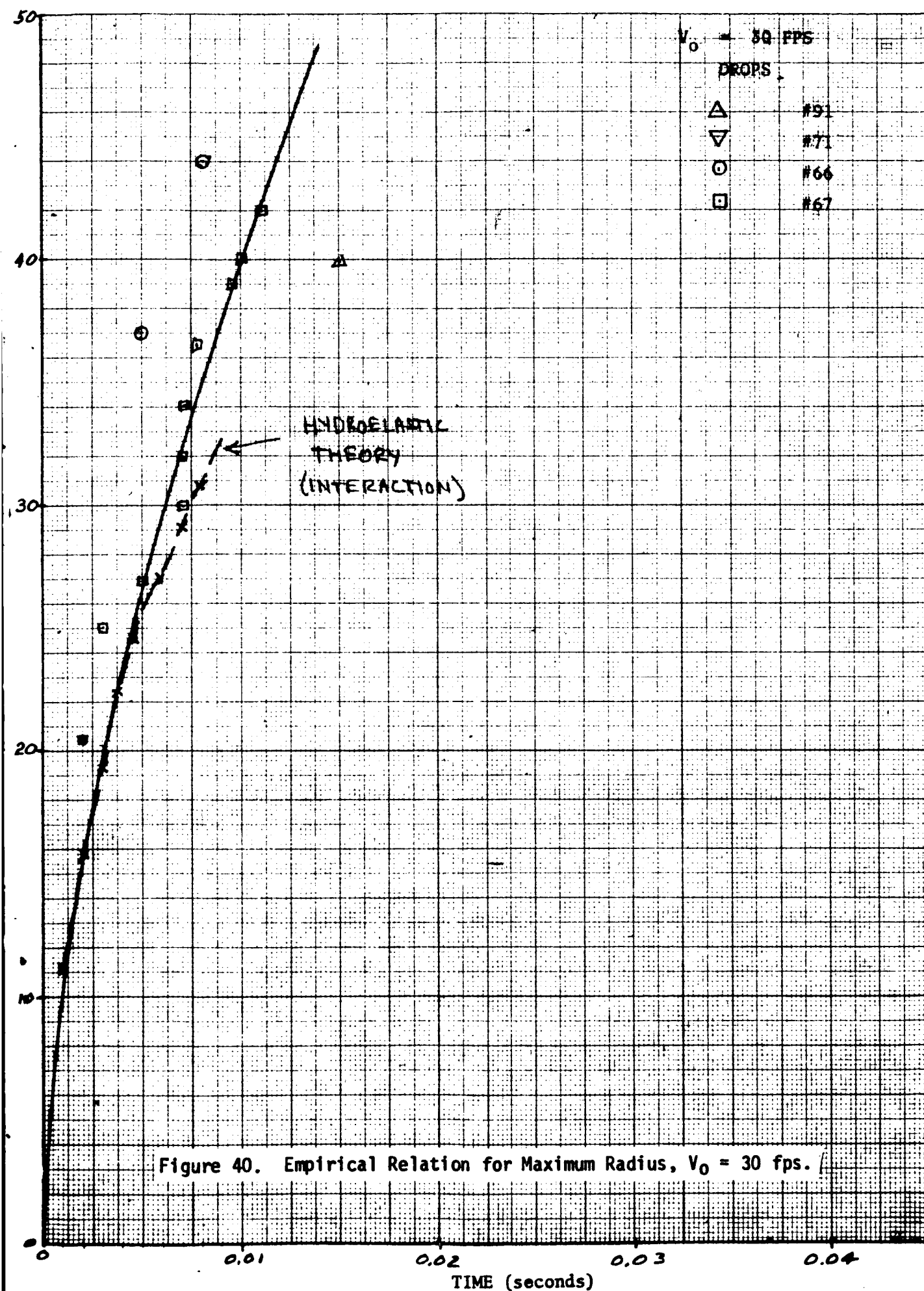Figure 31. Empirical Relation for Maximum Radius, V_0 = 16.5 fps.

Figure 32. Empirical Relation for Maximum Radius, V_o = 20.5 fps.
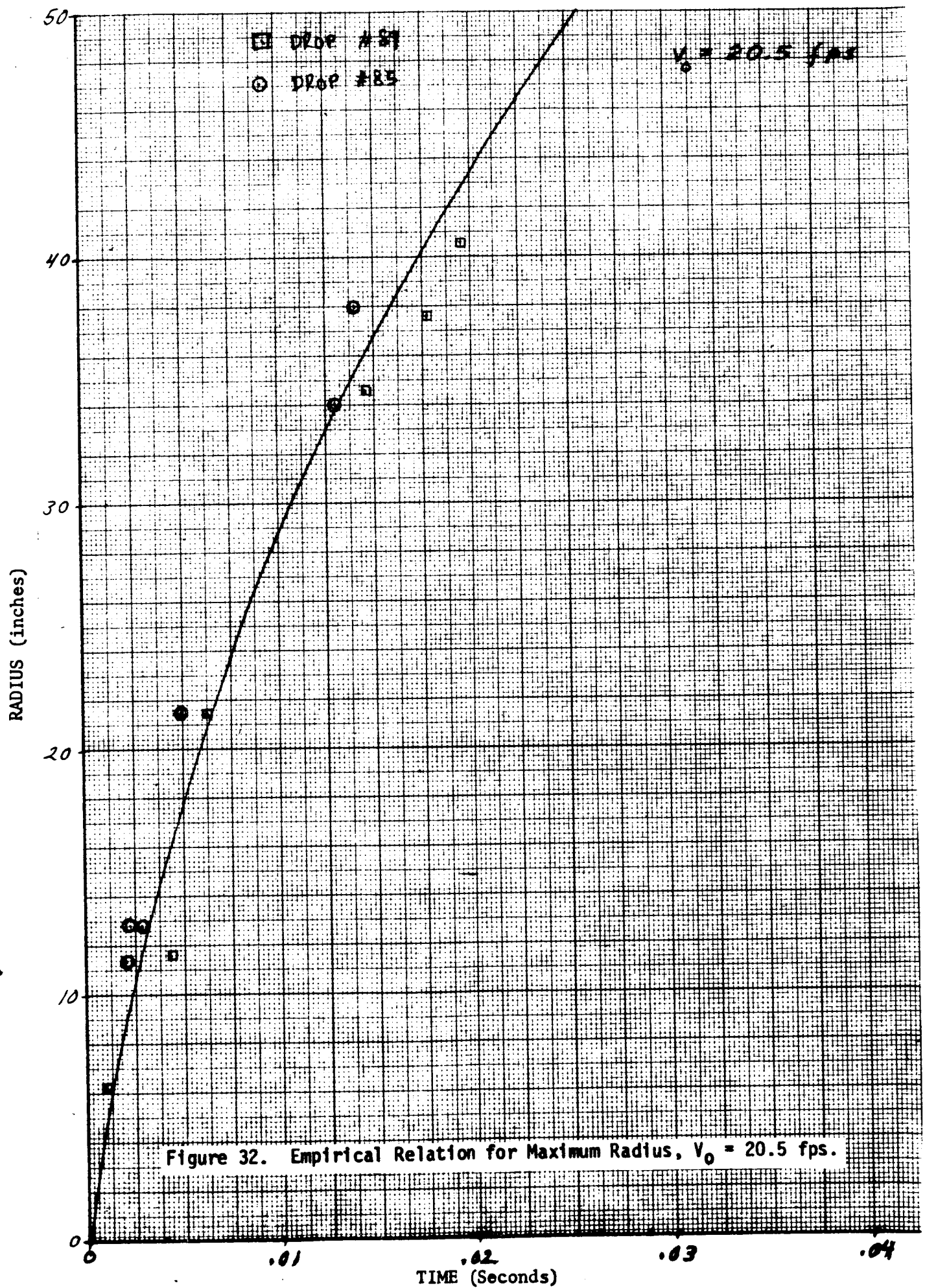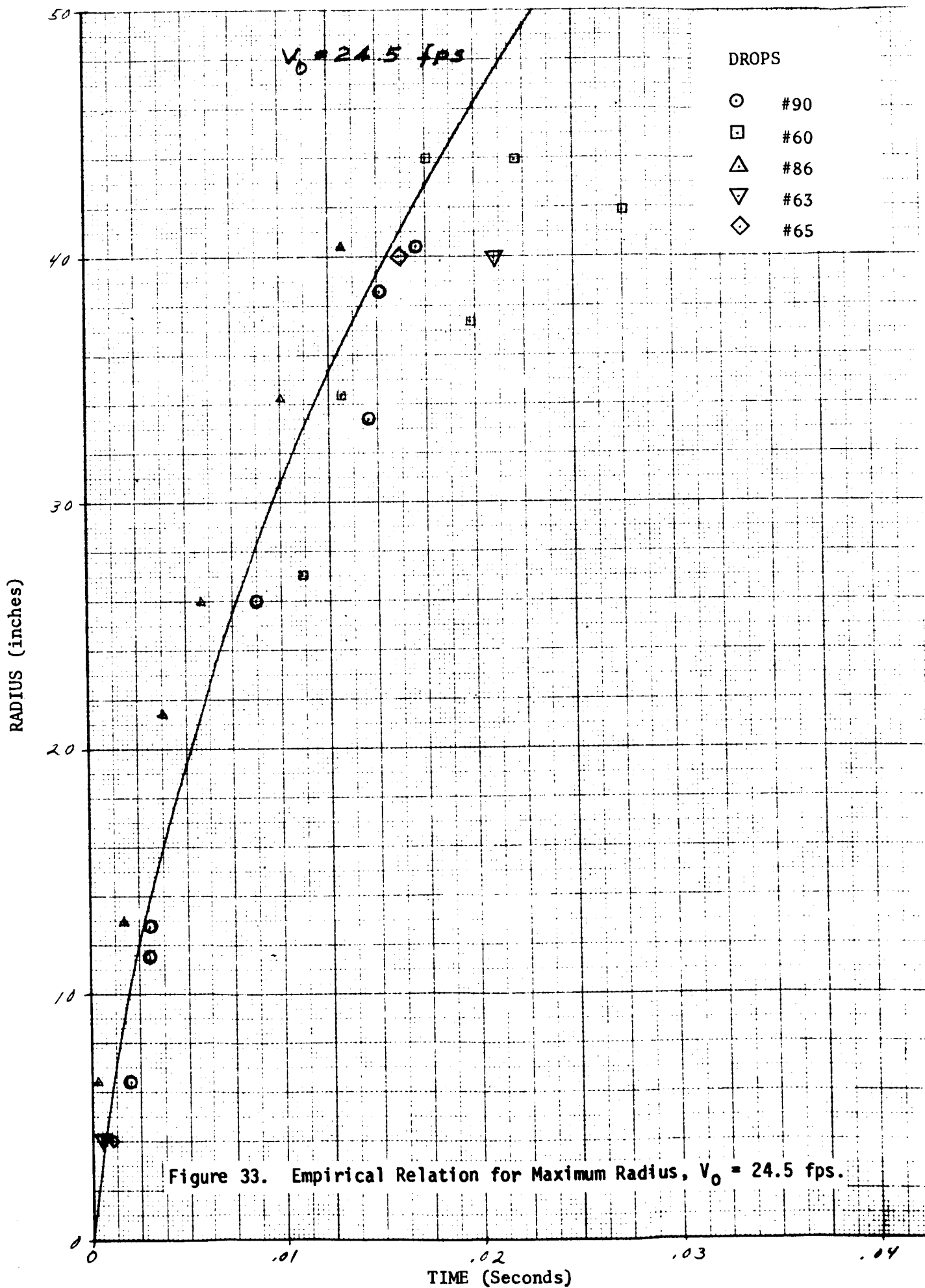
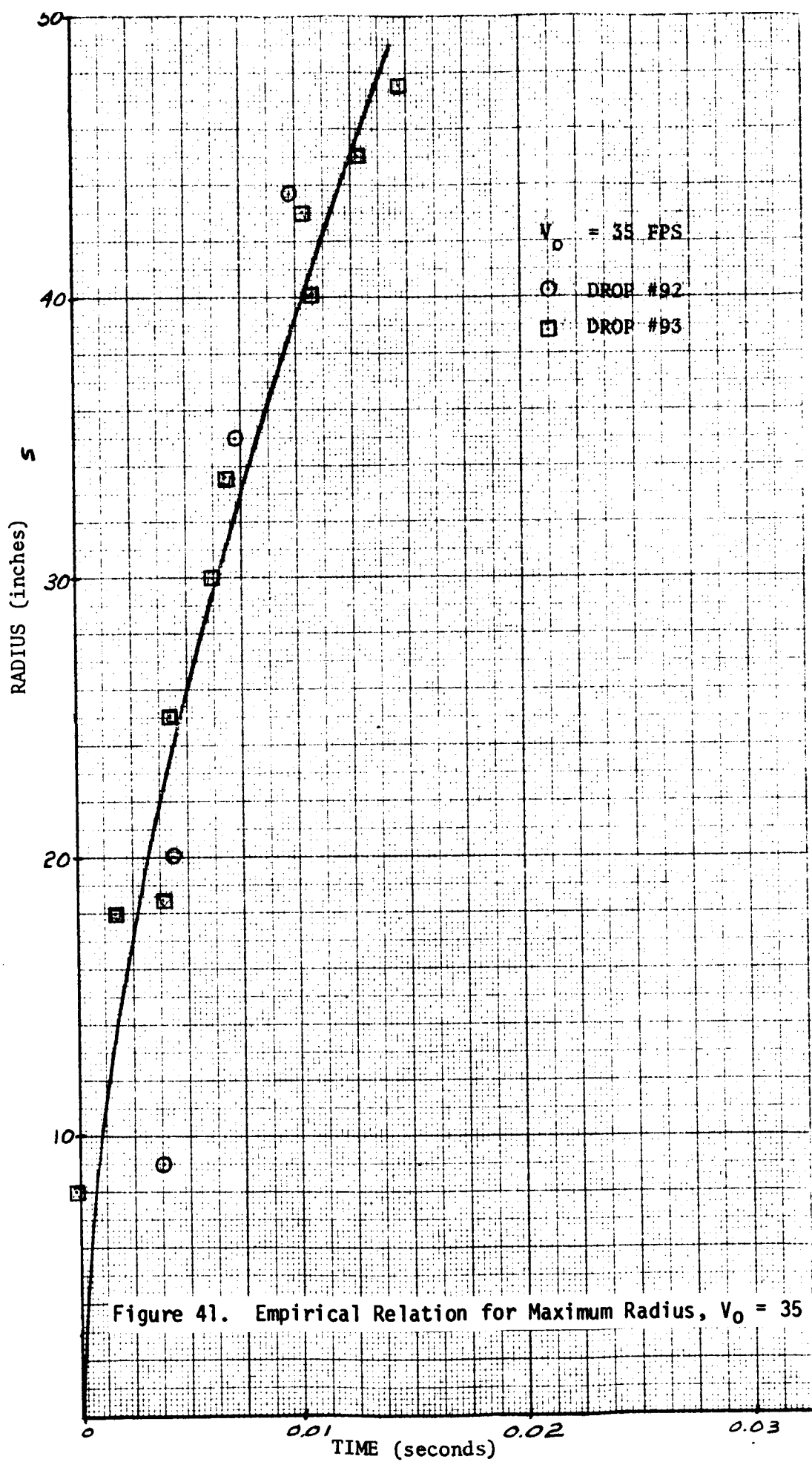Figure 33. Empirical Relation for Maximum Radius, V_0 = 24.5 fps.

Figure 34.   Empirical Relation for Maximum Radius, V_0 = 32 fps.

$$r_M = a_1 + Ta_2 + Va_3 + \ldots \ldots \quad (T = 1000t)$$

n	a_n	
1	− 7.7423	E00
2	4.8829	E00
3	2.1082	E00
4	− 1.7460	E-01
5	− 3.6744	E-01
6	− 1.7804	E-01
7	6.3465	E-03
8	− 1.4593	E-03
9	2.9865	E-02
10	6.4246	E-03
11	− 1.3472	E-04
12	1.4391	E-04
13	− 2.0984	E-05
14	− 9.2126	E-04
15	− 7.8470	E-05
16	1.3252	E-06
17	− 2.8625	E-06
18	3.0137	E-07
19	− 6.7121	E-07
20	1.1065	E-05
21	0.0	
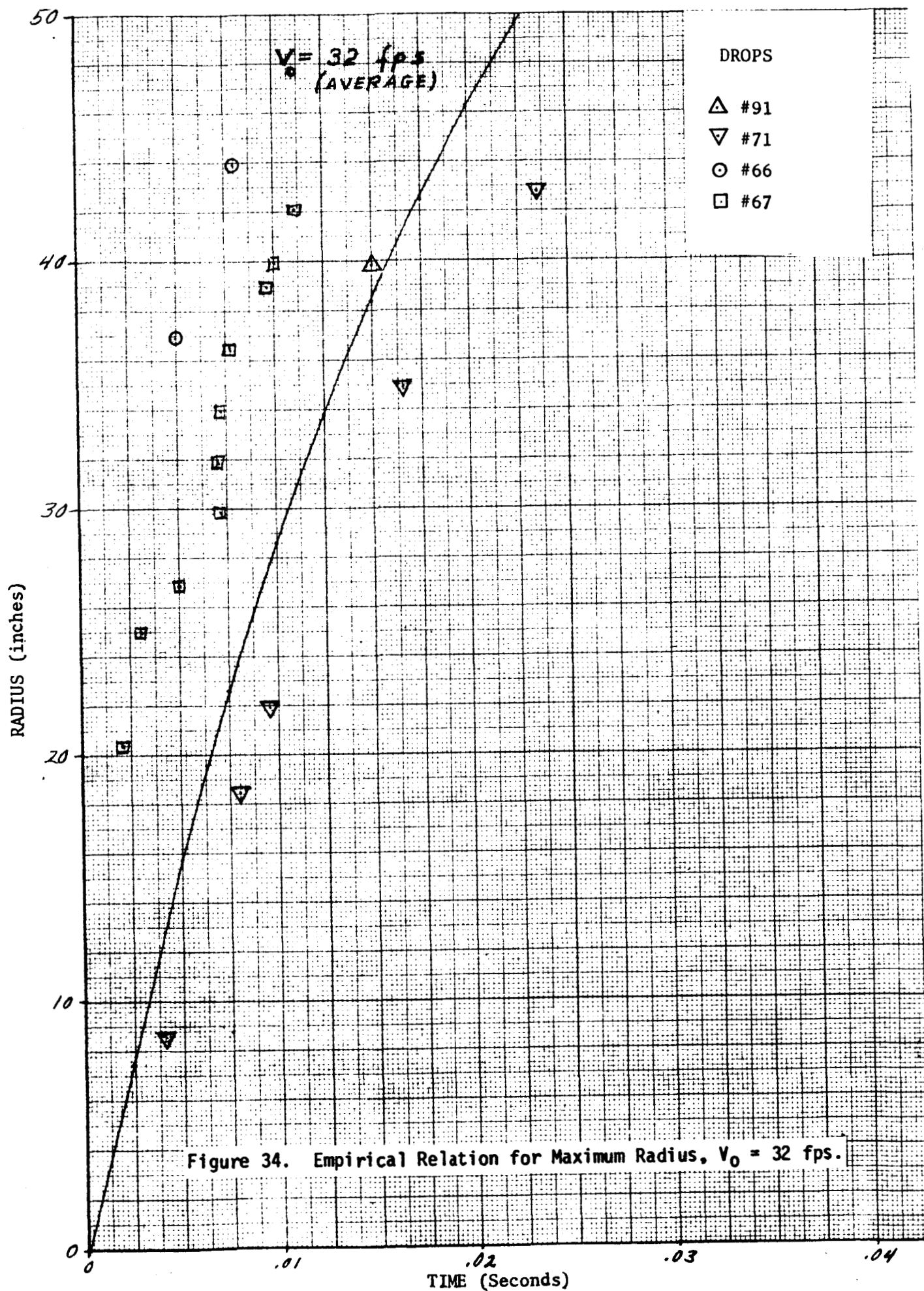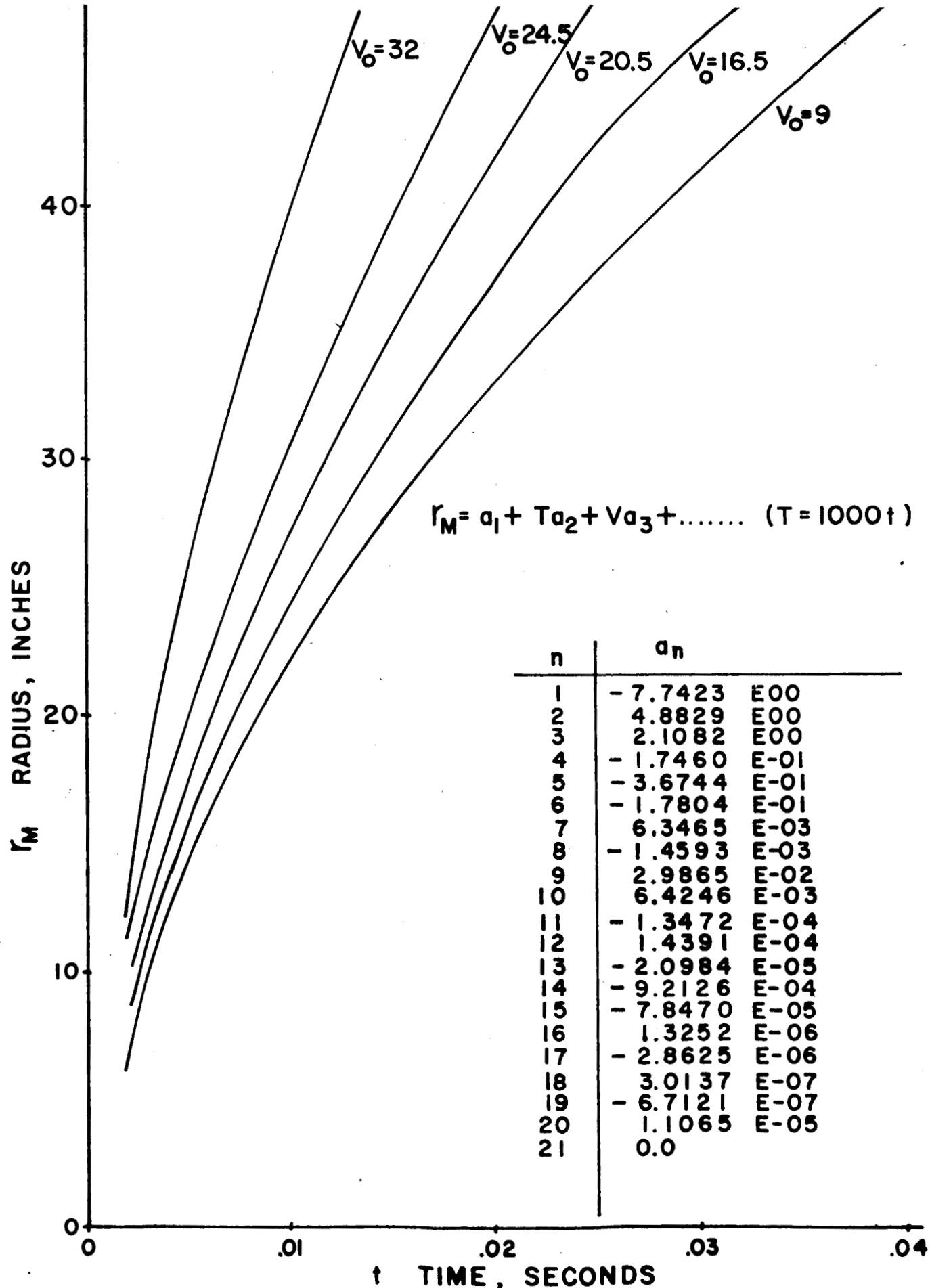
Figure 35.   Alternate Empirical Relation for Maximum Radius.

Figure 36. Empirical Relation for Maximum Radius, V_0 = 9 fps.
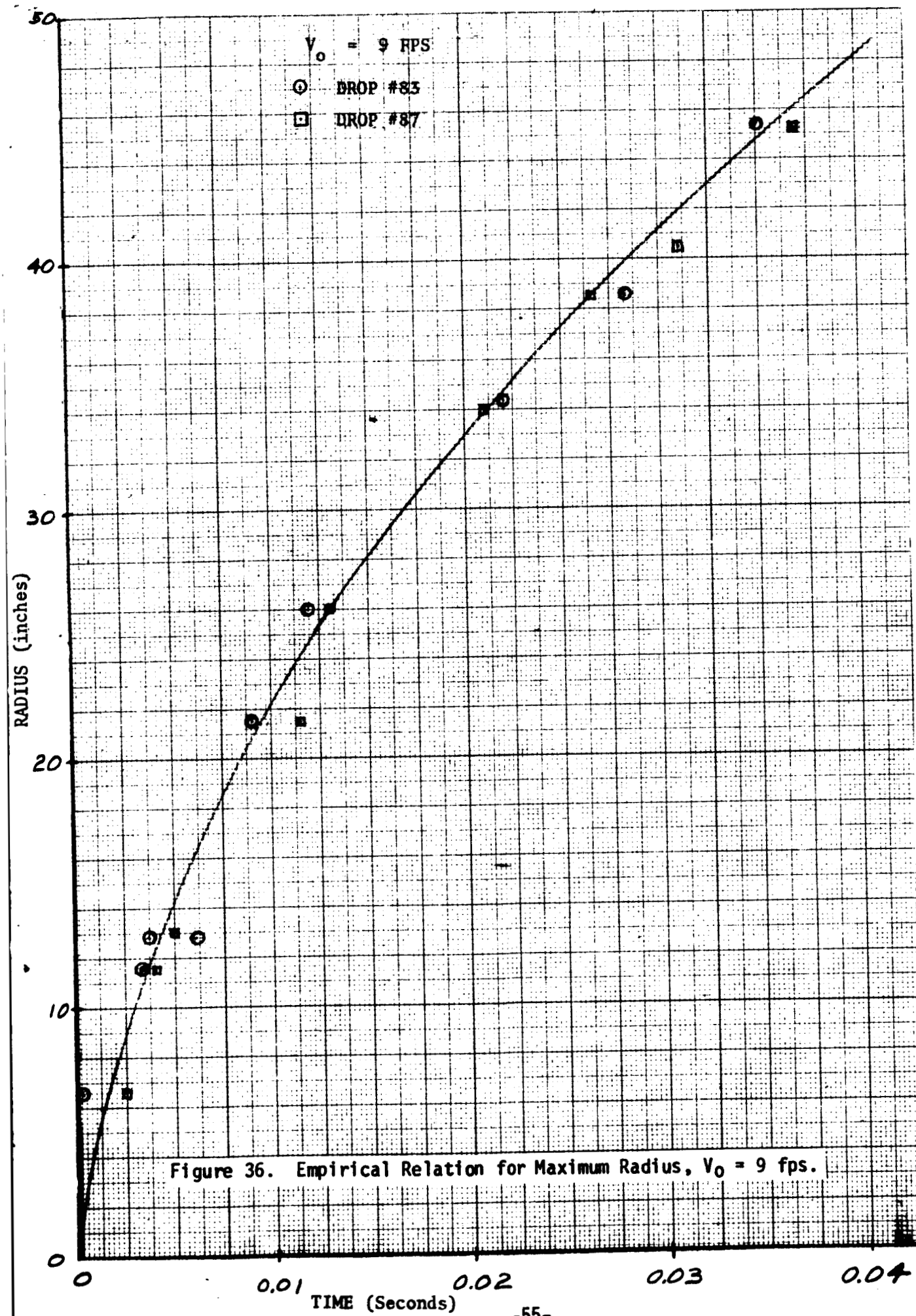
Figure 37. Empirical Relation for Maximum Radius, V_0 = 16.5 fps.

Figure 38. Empirical Relation for Maximum Radius, V_O = 20.5 fps.

Figure 39. Empirical Relation for Maximum Radius, V_0 = 24.5 fps.

Figure 40. Empirical Relation for Maximum Radius, V_0 = 30 fps.

Figure 41.   Empirical Relation for Maximum Radius, V_O = 35 fps.
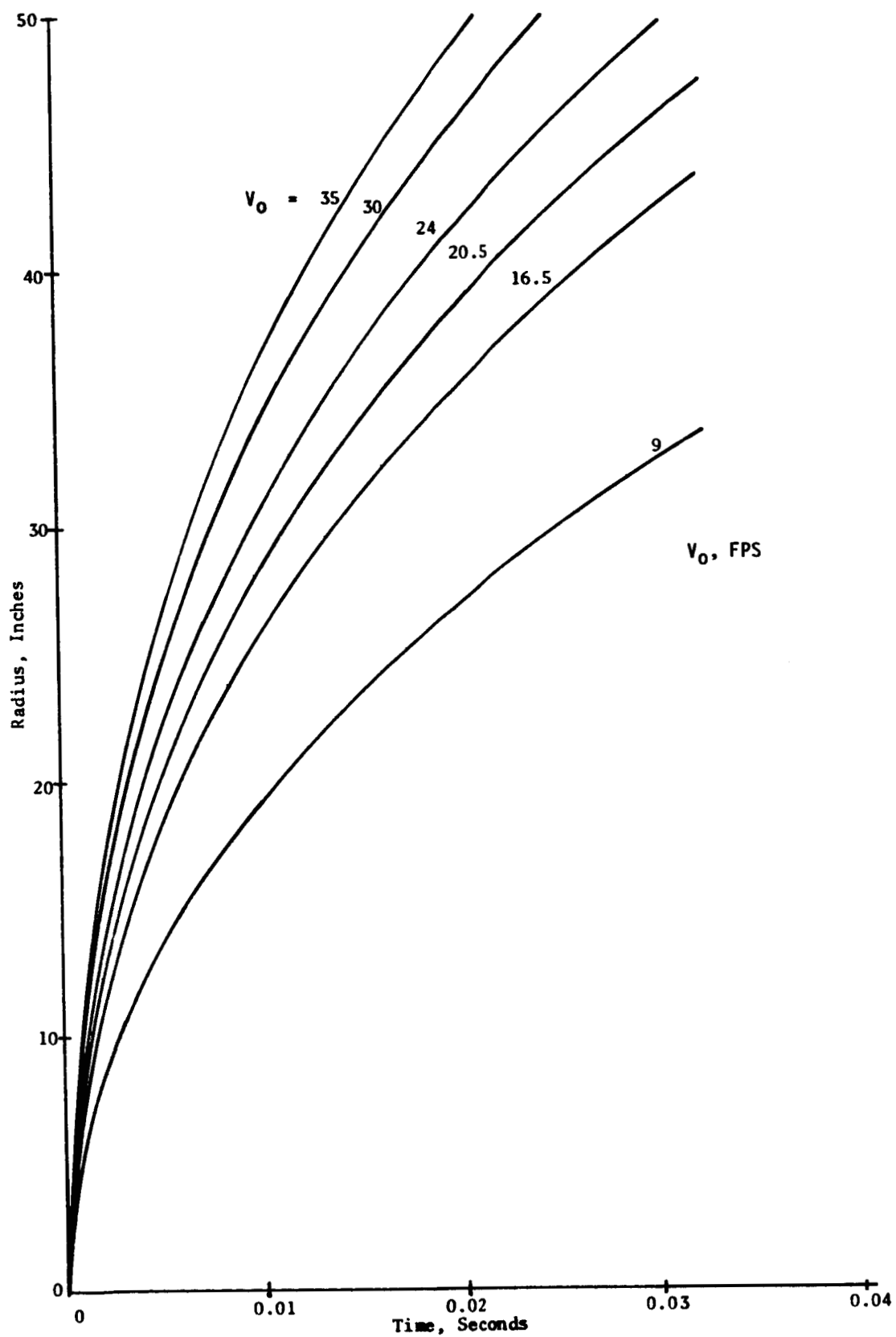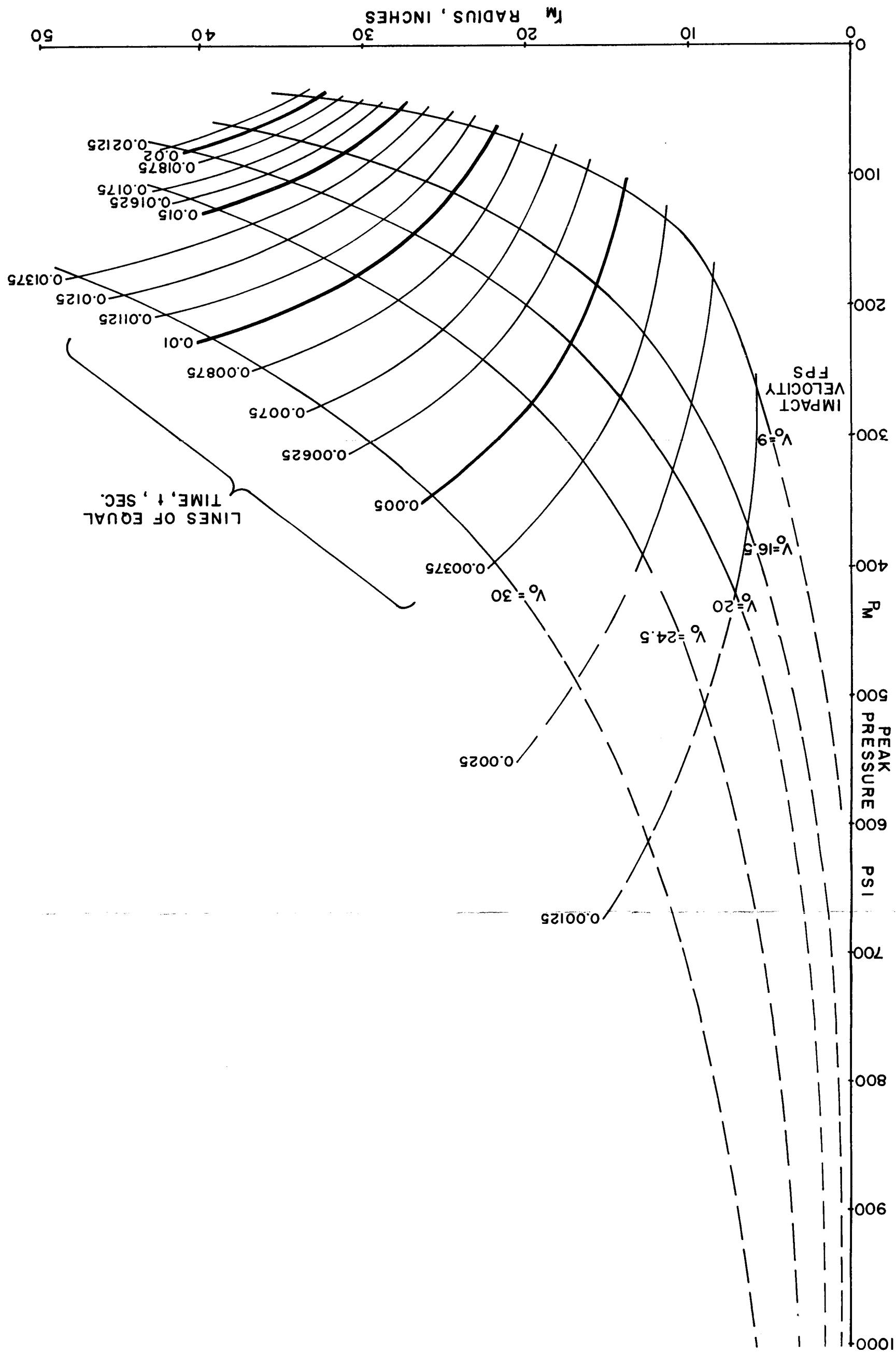
Figure 42. Radius by Rigid-Body Theory

Figure 43. Maximum Full-Scale Pressures as a Function of Time, Initial Impact Velocity, and Position.
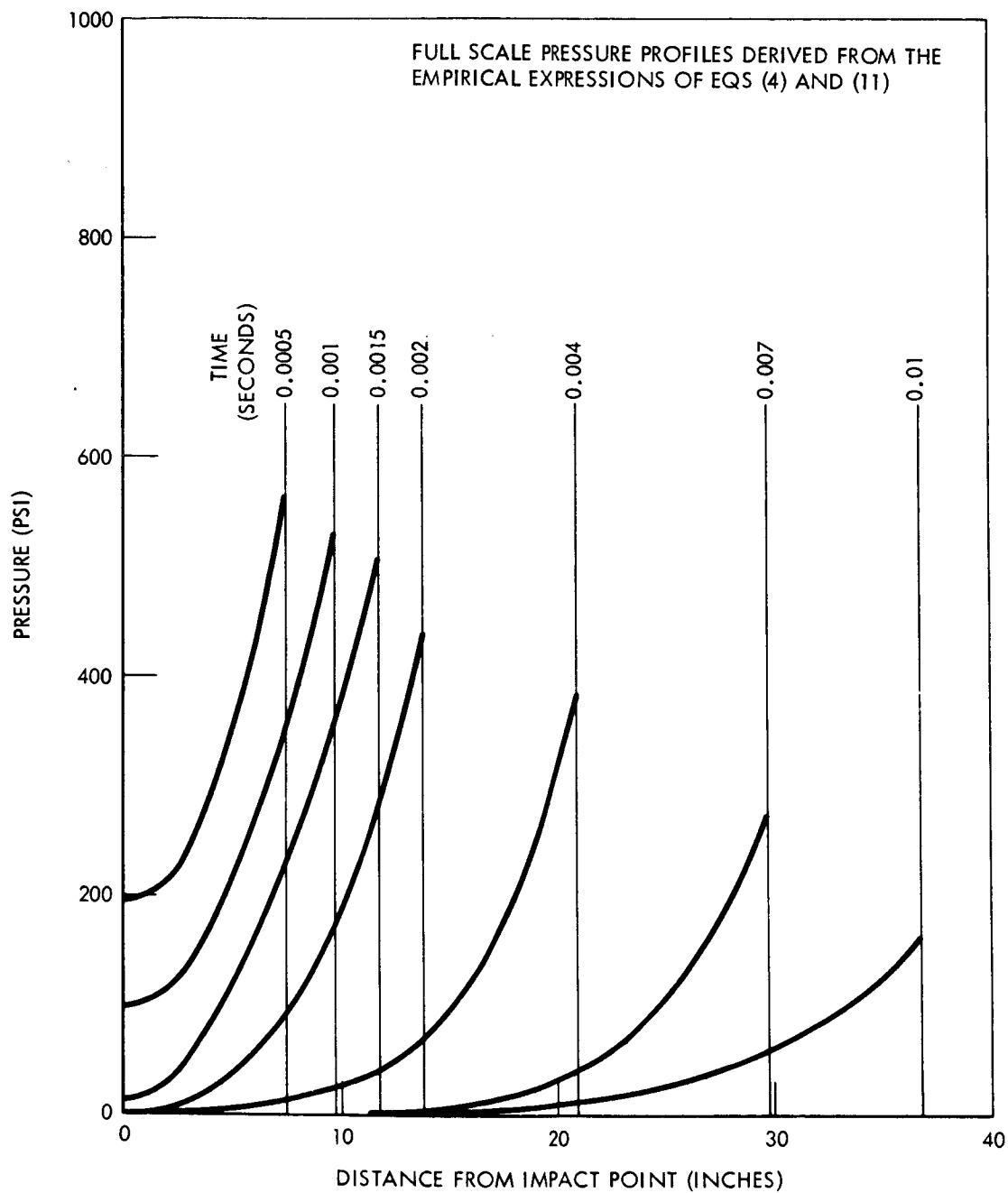
Figure 44. Empirically Derived Full Scale Pressure Profiles.
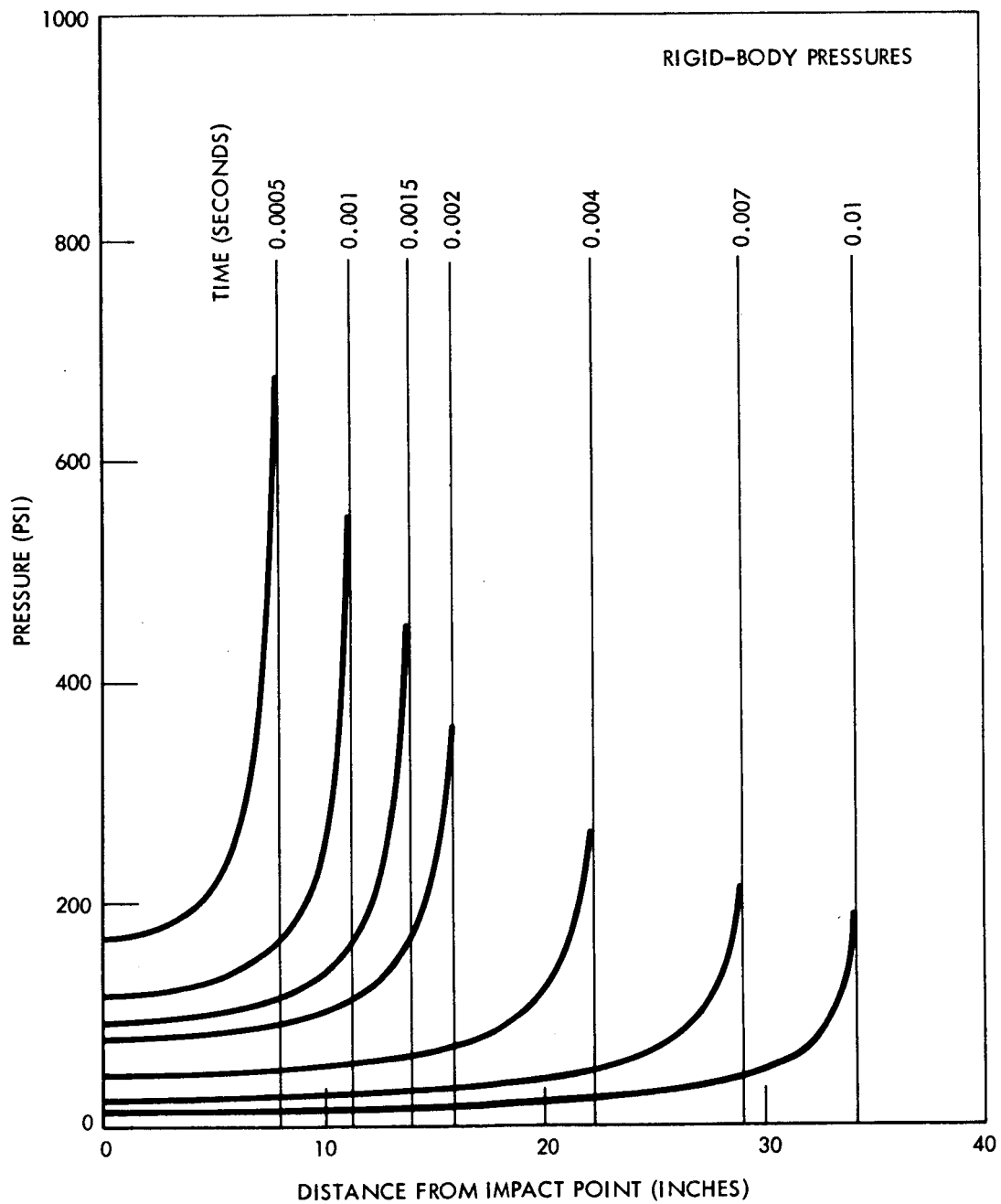
Figure 45. Pressure Profiles Derived From Rigid-Body Theory.
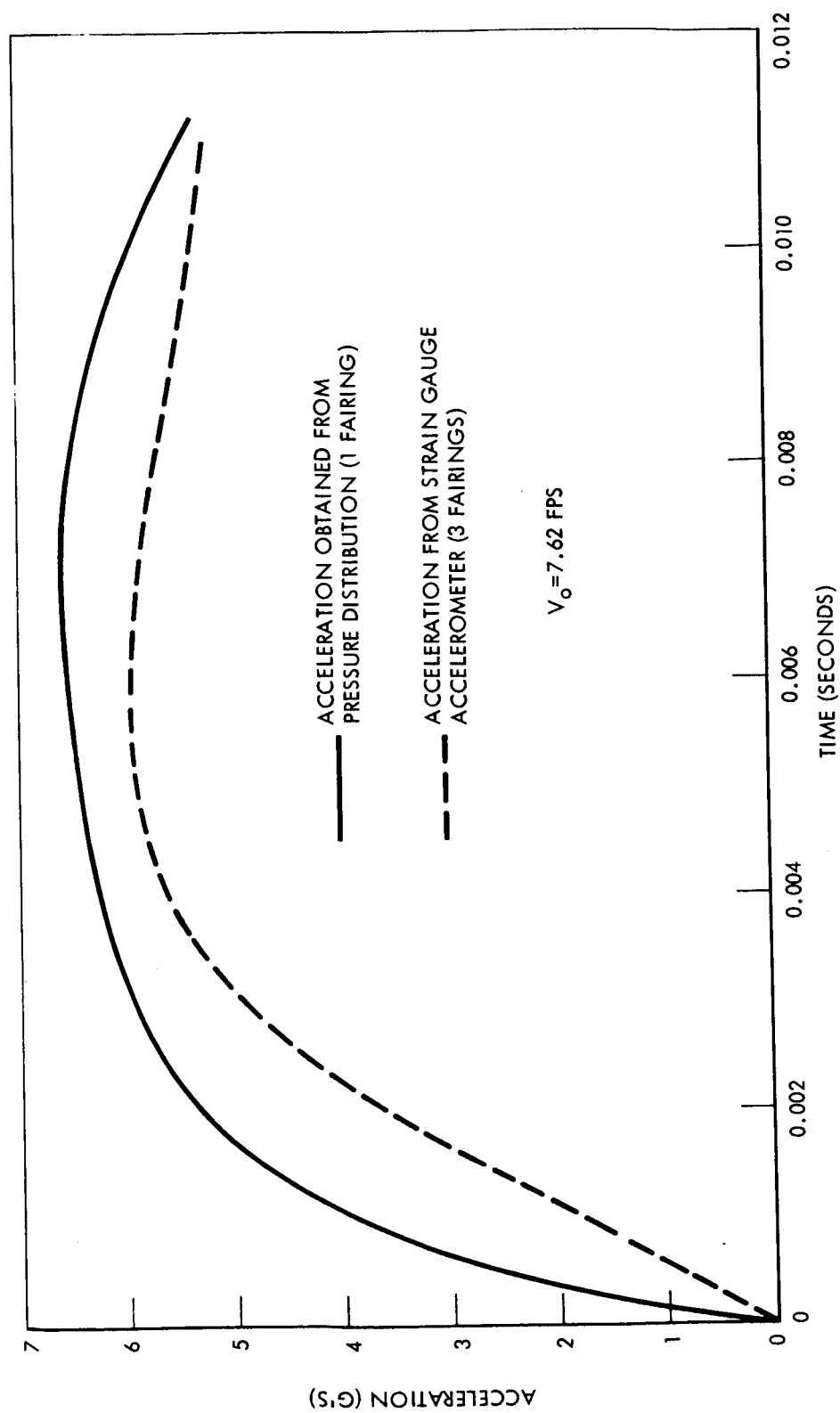
Figure 46. Quarter-Scale Experimental Accelerations.
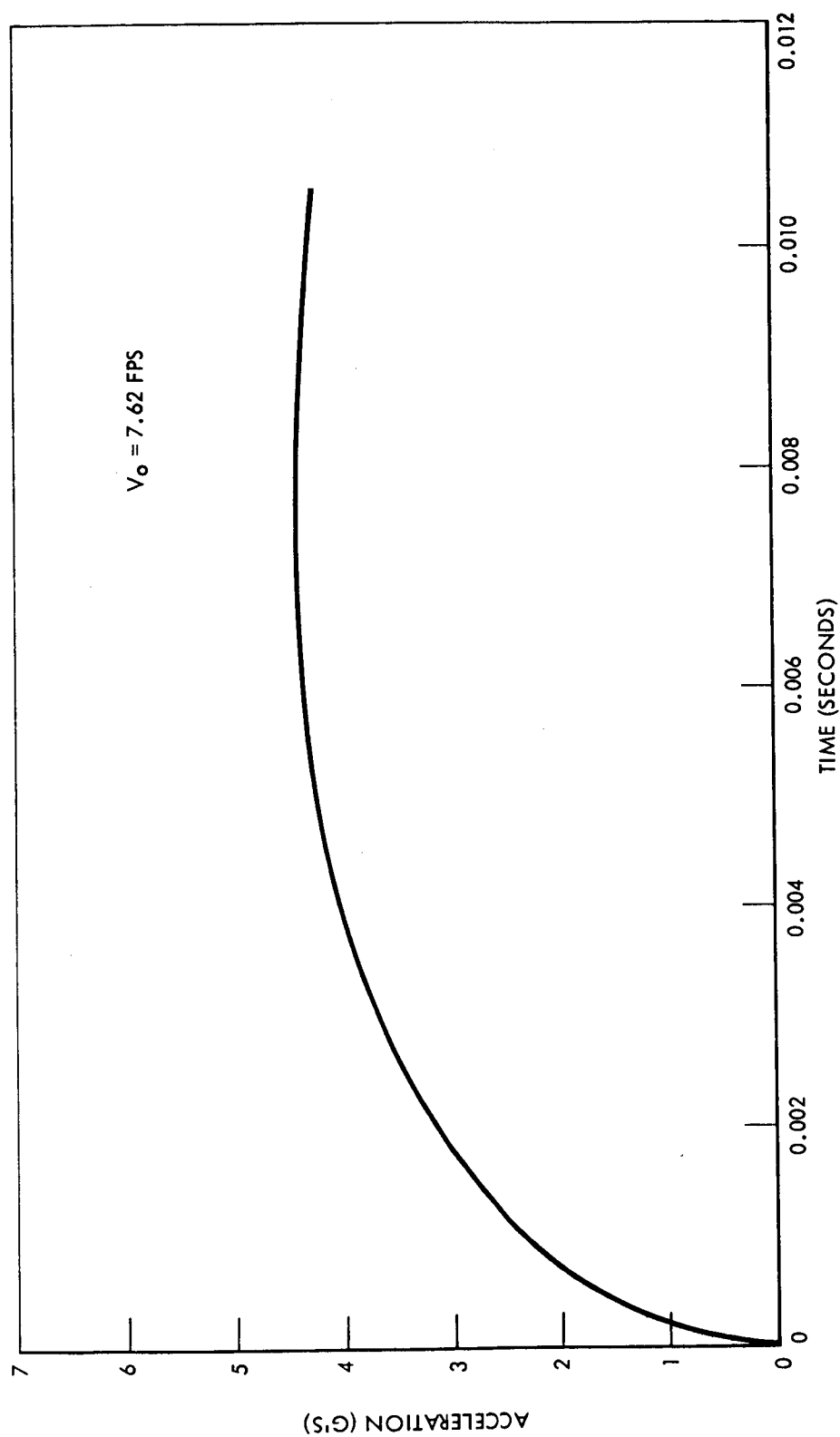
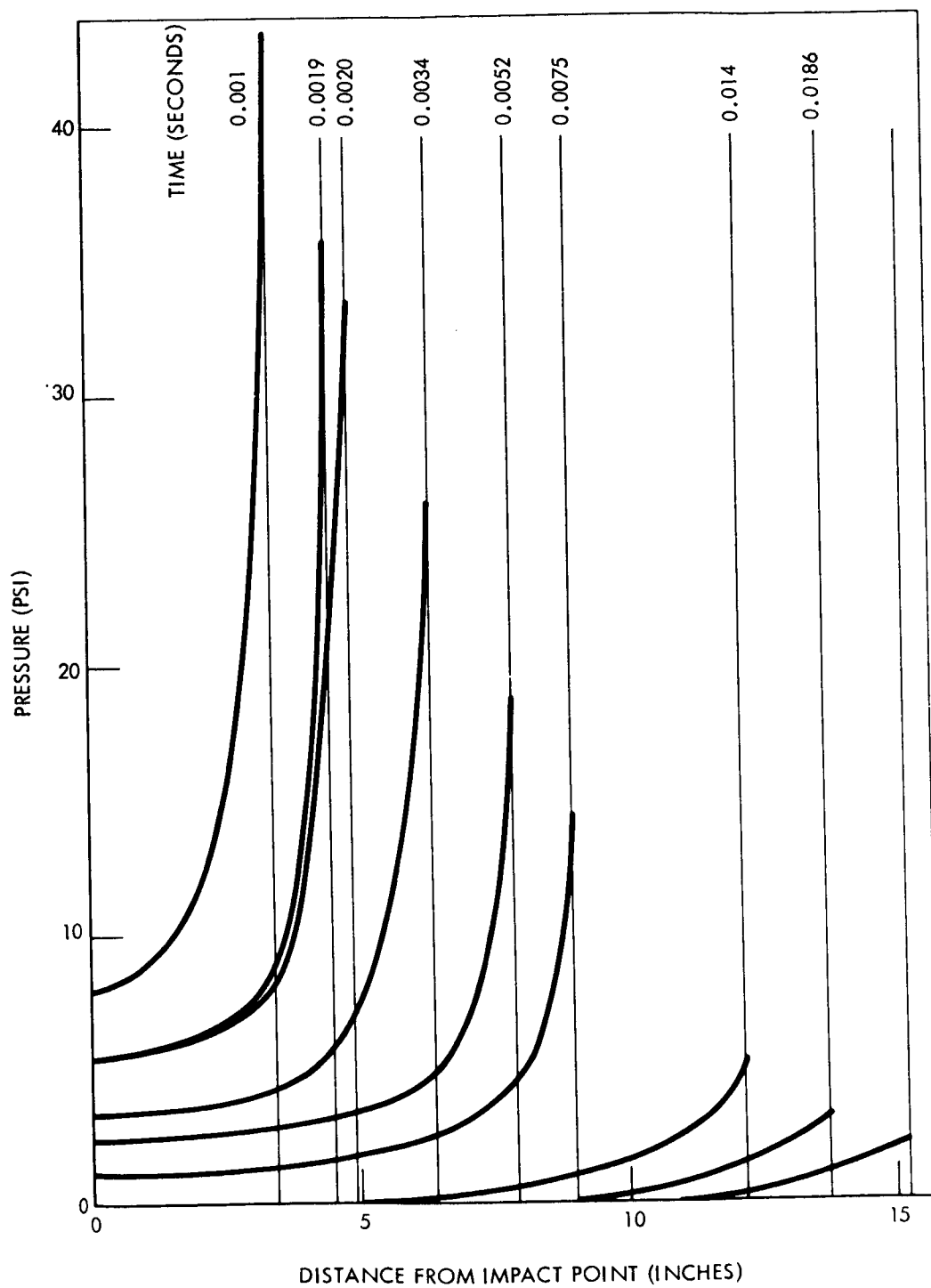Figure 47. Accelerations Predicted from Rigid-Body Theory.

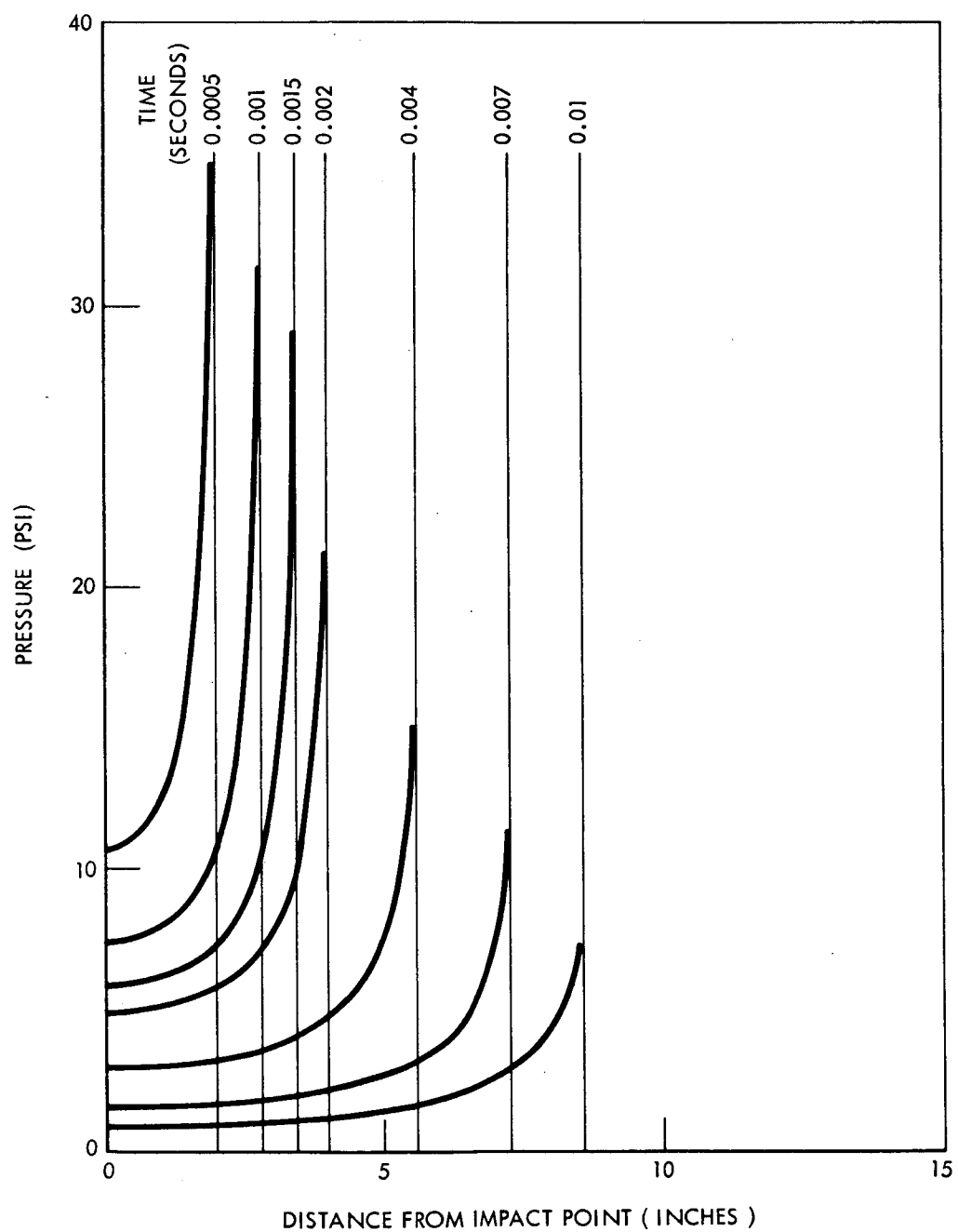Figure 48.   Pressure Profiles Predicted from Rigid-Body Theory, V_0=7.62 fps.

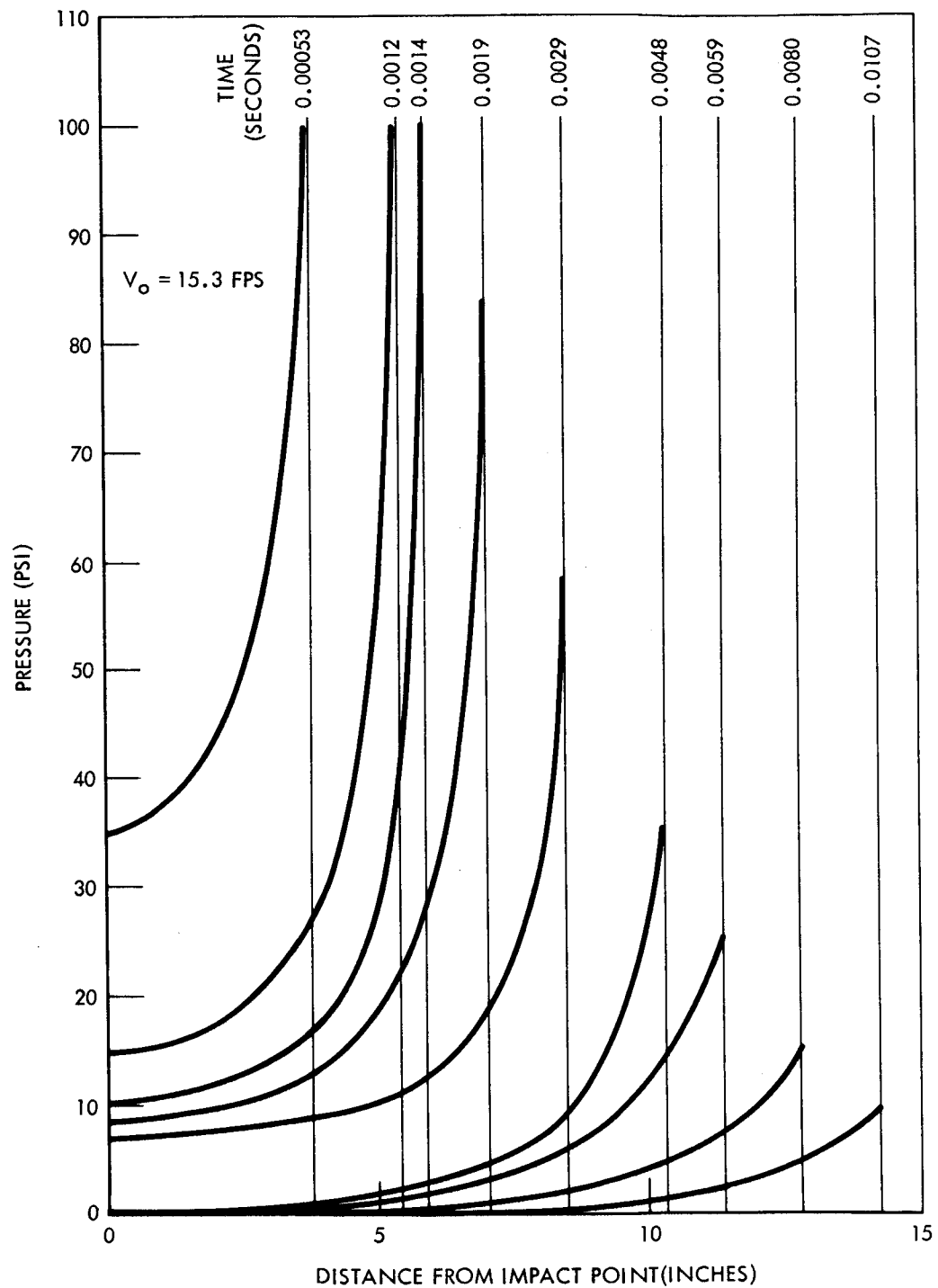Figure 49. Pressure Profiles Predicted from Rigid-Body Theory, V_o=7.62 fps.

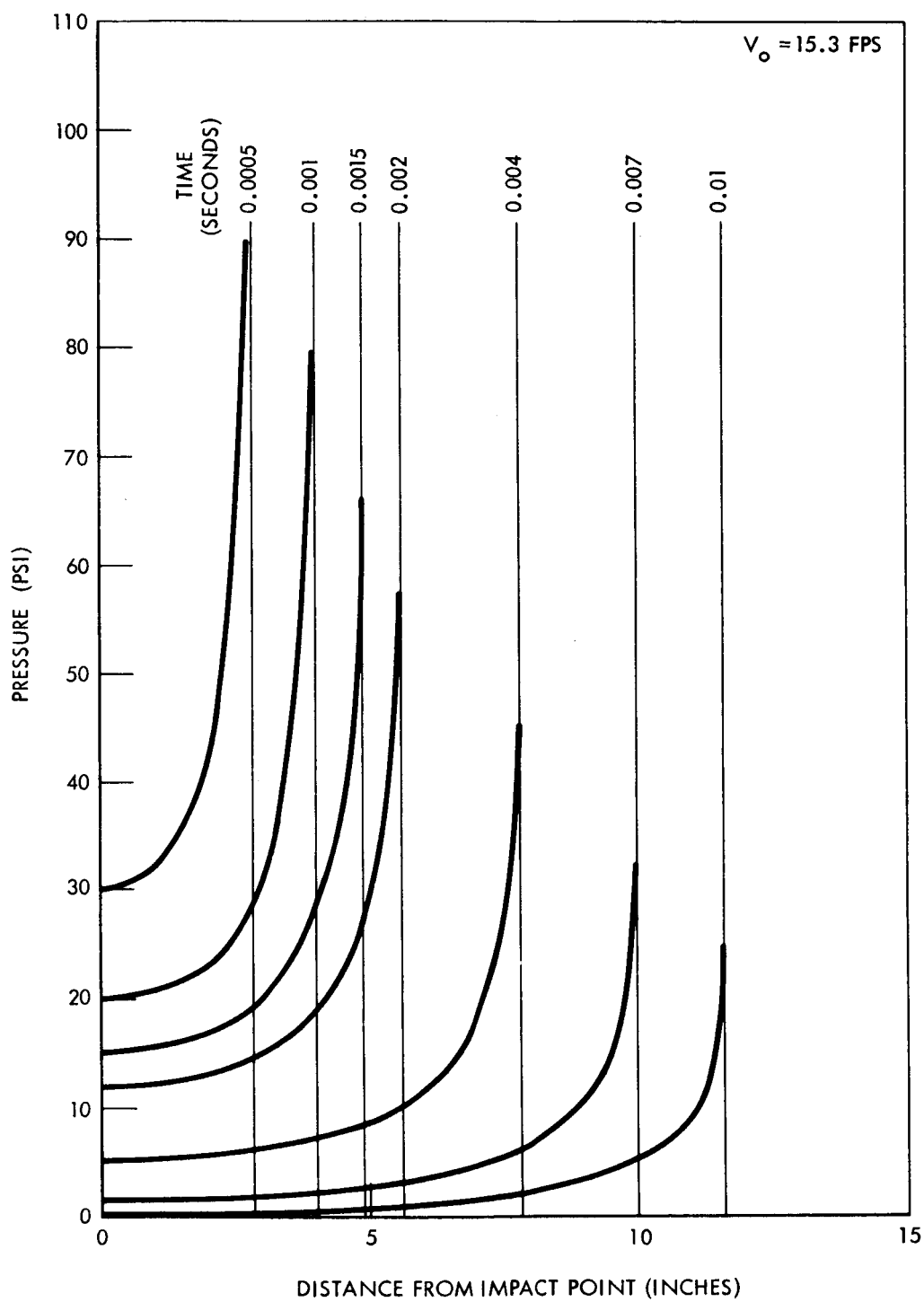Figure 50.   Quarter Scale Experimental Pressure Profiles, V_o = 15.3 fps.

Figure 51.   Pressure Profiles Predicted from Rigid-Body Theory, V_o=15.3 fps.